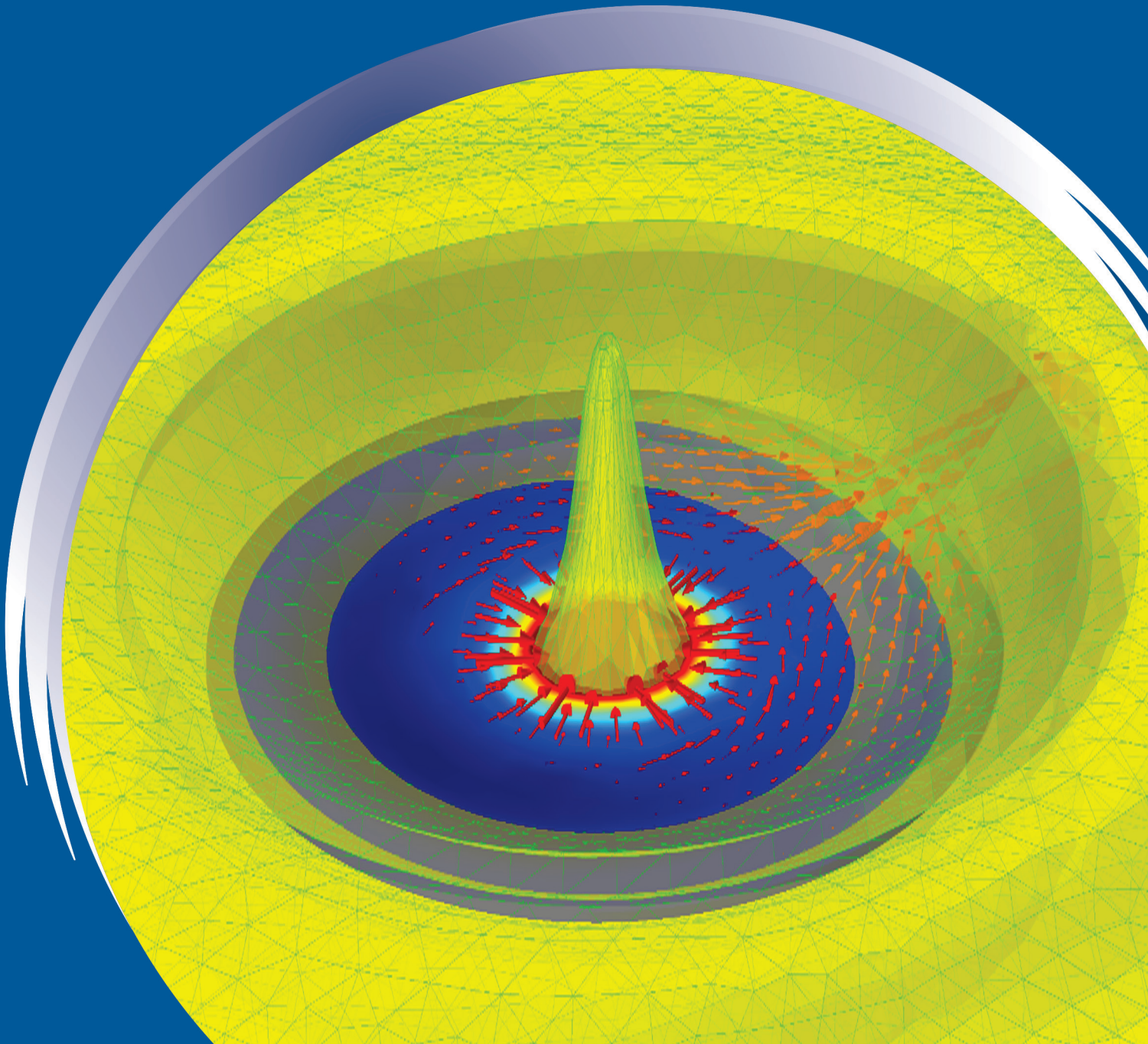


ISSN 0352-9045

# *Informacije* MIDEM

*Journal of Microelectronics,  
Electronic Components and Materials*  
**Vol. 47, No. 3(2017), September 2017**

*Revija za mikroelektroniko,  
elektronske sestavne dele in materiale*  
**letnik 47, številka 3(2017), September 2017**



# Informacije MIDE M 3-2017

Journal of Microelectronics, Electronic Components and Materials

VOLUME 47, NO. 3(163), LJUBLJANA, SEPTEMBER 2017 | LETNIK 47, NO. 3(163), LJUBLJANA, SEPTEMBER 2017

Published quarterly (March, June, September, December) by Society for Microelectronics, Electronic Components and Materials - MIDE M.  
Copyright © 2016. All rights reserved. | Revija izhaja trimesečno (marec, junij, september, december). Izdaja Strokovno društvo za mikroelektroniko, elektronske sestavne dele in materiale – Društvo MIDE M. Copyright © 2016. Vse pravice pridržane.

## Editor in Chief | Glavni in odgovorni urednik

Marko Topič, University of Ljubljana (UL), Faculty of Electrical Engineering, Slovenia

## Editor of Electronic Edition | Urednik elektronske izdaje

Kristijan Brecl, UL, Faculty of Electrical Engineering, Slovenia

## Associate Editors | Odgovorni področni uredniki

Vanja Ambrožič, UL, Faculty of Electrical Engineering, Slovenia

Arpad Bürmen, UL, Faculty of Electrical Engineering, Slovenia

Danjela Kuščer Hrovatin, Jožef Stefan Institute, Slovenia

Matija Pirc, UL, Faculty of Electrical Engineering, Slovenia

Matjaž Vidmar, UL, Faculty of Electrical Engineering, Slovenia

## Editorial Board | Uredniški odbor

Mohamed Akil, ESIEE PARIS, France

Giuseppe Buja, University of Padova, Italy

Gian-Franco Dalla Betta, University of Trento, Italy

Martyn Fice, University College London, United Kingdom

Ciprian Iliescu, Institute of Bioengineering and Nanotechnology, A\*STAR, Singapore

Małgorzata Jakubowska, Warsaw University of Technology, Poland

Marc Lethiecq, University of Tours, France

Teresa Orłowska-Kowalska, Wrocław University of Technology, Poland

Luca Palmieri, University of Padova, Italy

## International Advisory Board | Časopisni svet

Janez Trontelj, UL, Faculty of Electrical Engineering, Slovenia - Chairman

Cor Claeys, IMEC, Leuven, Belgium

Denis Donlagić, University of Maribor, Faculty of Elec. Eng. and Computer Science, Slovenia

Zvonko Fazarinc, CIS, Stanford University, Stanford, USA

Leszek J. Golonka, Technical University Wrocław, Wrocław, Poland

Jean-Marie Haussonne, EIC-LUSAC, Octeville, France

Barbara Malič, Jožef Stefan Institute, Slovenia

Miran Mozetič, Jožef Stefan Institute, Slovenia

Stane Pejovnik, UL, Faculty of Chemistry and Chemical Technology, Slovenia

Giorgio Pignatelli, University of Perugia, Italy

Giovanni Soncini, University of Trento, Trento, Italy

Iztok Šorli, MIKROIKS d.o.o., Ljubljana, Slovenia

Hong Wang, Xi'an Jiaotong University, China

## Headquarters | Naslov uredništva

Uredništvo Informacije MIDE M

MIDE M pri MIKROIKS

Stegne 11, 1521 Ljubljana, Slovenia

T. +386 (0)1 513 37 68

F. + 386 (0)1 513 37 71

E. [info@midem-drustvo.si](mailto:info@midem-drustvo.si)

[www.midem-drustvo.si](http://www.midem-drustvo.si)

Annual subscription rate is 160 EUR, separate issue is 40 EUR. MIDE M members and Society sponsors receive current issues for free. Scientific Council for Technical Sciences of Slovenian Research Agency has recognized Informacije MIDE M as scientific Journal for microelectronics, electronic components and materials. Publishing of the Journal is cofinanced by Slovenian Research Agency and by Society sponsors. Scientific and professional papers published in the journal are indexed and abstracted in COBISS and INSPEC databases. The Journal is indexed by ISI® for Sci Search®, Research Alert® and Material Science Citation Index™. |

Letna naročnina je 160 EUR, cena posamezne številke pa 40 EUR. Člani in sponzorji MIDE M prejema posamezne številke brezplačno. Znanstveni svet za tehnične vede je podal pozitivno mnenje o reviji kot znanstveno-strokovni reviji za mikroelektroniko, elektronske sestavne dele in materiale. Izdajo revije sofinancirajo ARRS in sponzorji društva. Znanstveno-strokovne prispevke objavljene v Informacijah MIDE M zajemamo v podatkovne baze COBISS in INSPEC. Prispevke iz revije zajema ISI® v naslednje svoje produkte: Sci Search®, Research Alert® in Materials Science Citation Index™.

## Content | Vsebina

<i>Original scientific paper</i>		<i>Izvirni znanstveni članki</i>
B. Pečar, M. Možek, D. Vrtačnik: Thermoplastic - PDMS Polymer Covalent Bonding for Microfluidic Applications	147	B. Pečar, M. Možek, D. Vrtačnik: Kovalentno spajanje termoplasta s PDMS polimerom za mikrofluidne aplikacije
G. Matič, M. Jankovec, M. Topič: Development and Evaluation of the Angular Response Measurement Setup for Solar Cells	155	G. Matič, M. Jankovec, M. Topič: Razvoj in ovrednotenje sistema za merjenje kotne odvisnosti sončnih celic
U. Prah, M. Wencka, Z. Kutnjak, M. Vrabelj, S. Drnovsek, B. Malic, H. Ursic: Multicaloric Effect in Polycrystalline $Pb(Fe_{0.5}Nb_{0.5})O_3$	165	U. Prah, M. Wencka, Z. Kutnjak, M. Vrabelj, S. Drnovsek, B. Malic, H. Ursic: Multikalorični pojav v polikristaliničnem $Pb(Fe_{0.5}Nb_{0.5})O_3$
S. Bernik, M. Podlogar, S. Rustja, M. Cergolj: Influence of Granulate and Pressure on Green Compacts and the Current-voltage Characteristics of Sintered ZnO-based Varistor Ceramics	171	S. Bernik, M. Podlogar, S. Rustja, M. Cergolj: Vpliv granulata in pritiska na zelene oblikovance in tokovno-napetostne karakteristike sintrane varistorske keramike na osnovi ZnO
H. Mercier, B. Malič, H. Uršič, D. Kuscer, F. Levassort Processing and Sintering of Sodium-potassium Niobate-based Thick Films:	179	H. Mercier, B. Malič, H. Uršič, D. Kuscer, F. Levassort: Priprava in sintranje debelih plasti na osnovi natrijevega kalijevega niobata
D. Berčan, A. Sešek, J. Trontelj: Design of Operational Transconductance Amplifier with Temperature Compensation	187	D. Berčan, A. Sešek, J. Trontelj: Načrtovanje operacijskega transkonduktančnega ojačevalnika s temperaturno kompenzacijo
Front page: Simulated Structural Deformation, Fluid Velocity and Pressure Distribution in PDMS-thermoplastic Microcylinder Pump. (B. Pečar et al.)		Naslovnica: Simulirana strukturna deformacija, hitrost fluida and porazdelitev tlaka v PDMS-termoplastični mikrocilindrski črpalki. (B. Pečar et al.)



# *Thermoplastic - PDMS polymer covalent bonding for microfluidic applications*

*Borut Pečar, Matej Možek and Danilo Vrtačnik*

*University of Ljubljana, Faculty of Electrical Engineering, Laboratory of Microsensor Structures and Electronics, Ljubljana, Slovenia*

**Abstract:** Two room-temperature bonding processes for thermoplastic - PDMS polymer covalent bonding based on the organic substrate surface functionalization by means of organofunctional silanes APTES and amine-PDMS linker were developed and applied. The efficiency of covalent bonding was evaluated by measuring water contact angles on oxygen plasma pretreated surfaces and by measuring burst pressure on fabricated test devices. Developed amine-PDMS linker bonding process resulted in bond strength of 5 bar and 2 bar on continuous pressure of air and water respectively, while water initiated the hydrolysis of covalent bonds established via the modified APTES bonding process. Both bonding processes were applied on piezoelectric micropumps where glass substrate was replaced by thermoplastic substrate. Micropumps employing amine-PDMS linker exhibit no deterioration in their performance after eight weeks of continuous operation.

**Keywords:** PDMS; WCA; APTES; thermoplastics; covalent bonding; micropump

## *Kovalentno spajanje termoplasta s PDMS polimerom za mikrofluidne aplikacije*

**Izvleček:** Raziskali, razvili in vpeljali smo dva nizko temperaturna postopka kovalentnega spajanja termoplasta in PDMS polimera, ki temeljita na funkcionalizaciji organske površine preko organofunkcionalnega silana APTESa in amino-PDMS povezovalca. Učinkovitost površinske aktivacije, ki je ključna za učinkovit kovalenten spoj, smo ovrednotili z merjenjem omakalnih kotov vodnih kapelj na površini vzorcev pred in po aktivaciji površin v kisikovi plazmi. Za ovrednotenje kvalitete spoja smo na namensko izdelanih testnih čipih izvedli tlačne in porušitvene teste. Amino-PDMS povezovalac je zagotovil obstojnost spoja ob stiku z vodo, medtem ko so vezi vzpostavljene preko APTESa kljub dodatni toplotni obdelavi po nanosu in modifikaciji parametrov plazemske aktivacije površin razpadle. Razvita postopka spajanja smo vpeljali v proces izdelave piezoelektričnih mikročrpalk. Piezoelektrične mikročrpalke izdelane s postopkom amine-PDMS povezovalca po osmih tednih neprekinjenega delovanja ne izkazujejo upada pretočne zmogljivosti.

**Ključne besede:** PDMS; WCA; APTES; termoplast; kovalentno spajanje; mikročrpalka

\* Corresponding Author's e-mail: borut.pecar@fe.uni-lj.si

### *1 Introduction*

Plastics are indispensable in mass production of microfluidic devices due to their robustness, light weight, optical transparency, simplicity of molding and cost efficiency [1]. Plastics rigidity enables a variety of reliable external interface options, such as manifold integration, direct barbed tubing connections, and gasket connectors [2]. In addition, thermoplastic (TP)-polydimethylsiloxane (PDMS) assemblies have a number of advantages over homogeneous assemblies. The combined surface properties of the two materials, for example, could provide an optimal environment for con-

ducting cell-based research necessitating precise fluid control for targeted cell or biomolecule immobilization [3].

Many strategies for plastic-PDMS bonding have been previously reported, such as sol-gel coating approach, chemical gluing approach and organofunctional silanes approach [4, 5]. First approach requires multiple coating procedures as well as complex technology. Second approach creates chemically robust amine-epoxy bonds at the interface at room temperature, however, two silane-coupling reagents are required and both

surfaces had to be oxidized prior to chemical modification. Third approach requires only one coupling agent. In this approach, the most widely used organofunctional silane is 3-amino propyltriethoxysilane (APTES), aminosilane frequently employed in covalent bonding of organic films to metal oxides [6].

However, TP-PDMS covalent bonds established via organofunctional silanes are prone to degradation over prolonged period in aqueous environment which might limit the use in specific microfluidic applications.

Few studies attempted to increase hydrolytic stability of APTES by mixing it with complex agents such as BTISPA, BTMSPA, BTESE [2] or GPTMS [7]. Hydrolytic resistance of APTES mixed with BTISPA improved to hydrolytically stable bonds over a range of 0 to 15 pH when BTISPA was prevailing in the mixture. Authors attributed increased hydrolytic resistance to the greater cross-link density for bis-silanes. APTES mixed with GPTMS yielded higher bond strength as compared to APTES, but did not improved hydrolytic stability [8].

Being aware of reported limited hydrolytic resistance of APTES [2, 7], we tried to introduce additional post-deposition heat treatment and modification of post-deposition plasma treatment that might overcome this disadvantage and provide the bond strength sufficient for specific application e. g. in the range of 0.5-0.7 bar. The advantages of employing APTES linking agent include easy availability of the product and well established bonding process due to substantial popularity in microfluidic community.

In this work, approach of employing two organofunctional silanes, APTES and poly [dimethyl siloxane-co-(3-aminopropyl) methyl siloxane (amine-PDMS linker) for bonding PDMS elastomer to TP substrates via methanol aligning medium was developed and applied. Amine-PDMS linker incorporates an amine functionality at one terminal and a segment of low molecular weight PDMS at the other, which might provide better hydrolytic bond stability [3]. Surface properties of TPs and PDMS were analyzed by measuring the water contact angles (WCA). The bond strength and bond hydrolytic stability were evaluated by delamination and burst pressure tests. Both bonding processes were further improved and applied on piezoelectric micropumps, where supporting bottom glass was replaced by TP substrate.

## 2 Experimental

### 2.1 Materials

In the presence of amine in organofunctional aminosilane bonding process, thermoplastics undergo

aminolysis followed by chain scission of the carbonyl backbone, forming a strong urethane bond. Therefore, not all thermoplastics, but only thermoplastics that can undergo aminolysis are suitable for the purpose. For TP substrates, optically transparent 2 mm thick Polycarbonate (PC), Acrylonitrile butadiene styrene (ABS) and Poly methyl methacrylate (PMMA) from INEOS Styrolution Group GmbH were employed.

In all experiments, a PDMS Sylgard® 184 two-part kit consisting of a pre-polymer (base) and a cross-linker (curing agent) from Dow Corning Corporation mixed at a ratio 10:1 was applied. For surface functionalization of plastic substrates, a commercial solution of APTES (Sigma Aldrich) and amine- PDMS linker (Sigma Aldrich) were used. In bonding processes, methanol and DI of technical purity were applied.

### 2.2 Surface wettability measurements

As argued by Garbassi et al. [9], the oxidation of the surface layer increases the concentration of hydroxyl groups which leads to the formation of strong intermolecular bonds. As the silanol groups are polar in nature, they make the exposed surface highly hydrophilic and this can be observed by measuring WCAs [10]. Those WCAs were found in direct correlation with bond strength [11].

For WCA determination a method was developed which included photographing of droplets on inves-

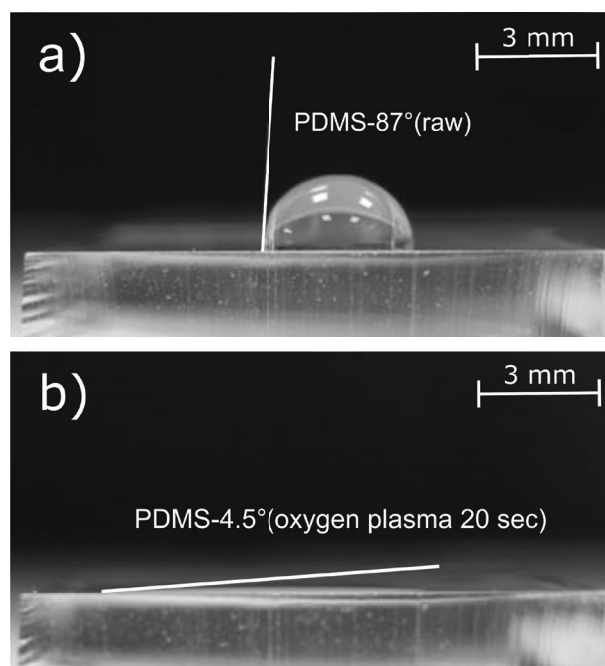


**Figure 1:** Micrograph (camera Nikon e990) of water droplet on raw PDMS surface (a) and on oxygen plasma treated PDMS surface (b).

tigated surfaces. The images of the droplet were analyzed by computer software “ImageJ” and “ContactAngle” plugin from points marked along the droplet-air interface to calculate the contact angle at the droplet-surface interface.

An example of WCA measurement on raw PDMS and on PDMS treated in oxygen plasma (20 sec, 0.8 mbar, 40W) is shown in Fig. 1. For all plasma treatments, ATTO Low Pressure Plasma Systems Diener electronic GmbH was employed.

### 2.3 Bonding process

In order to overcome reported limited hydrolytic resistance of APTES [2, 7], additional post-deposition heat treatment and modification of post-deposition plasma treatment were introduced in the bonding process. The process flow for TP-PDMS sandwich covalent bonding is schematically shown in Fig. 2. First, TP substrates were cleaned in ultrasonic bath, followed by silylation of the surfaces through the use of organofunctional silanes. In order to achieve good adhesion, TPs were pre-activated in oxygen plasma, resulting in the hydrophilization of the TP surfaces.

TP sheets were then immersed in the APTES (5% per volume) or coated with amine-PDMS linker and addi-

tionally heated to 60 °C for 20 min. Such an additional post-deposition heating step was expected to increase the number of established urethane bonds, especially between TP and APTES where bonds are prone to hydrolytic decay. Unlinked organofunctional silanes were washed away with isopropyl alcohol in ultrasonic bath. Both PDMS and functionalized TP substrate surfaces were again activated in the oxygen plasma. Post-deposition plasma treatment was prolonged to 1 min at increased pressure of 2 mbars and increased power of 50 W in order to increase the formation of Si–OH groups on both surfaces (Fig. 2 b). For all further oxygen plasma treatments, modified parameters were employed.

After plasma activation, the activated surfaces of the two substrates were brought into contact, using methanol as an aligning medium (Fig. 2 b). After methanol evaporation, covalent bonds were formed which were then additionally stabilized by curing at 80°C for 1 h in laboratory furnace.

### 2.4 Characterization of the bond strength

The bond strength was evaluated by performing delamination and burst pressure tests. Fig. 3 shows PDMS residues on ABS substrate after the PDMS elastomer was delaminated. In this particular case, APTES was employed as a linking agent. It was presumed that the area of PDMS residues left on the TP surface was directly related to bond strength. No obvious correlation between TP type and bond strength was found by delamination tests.

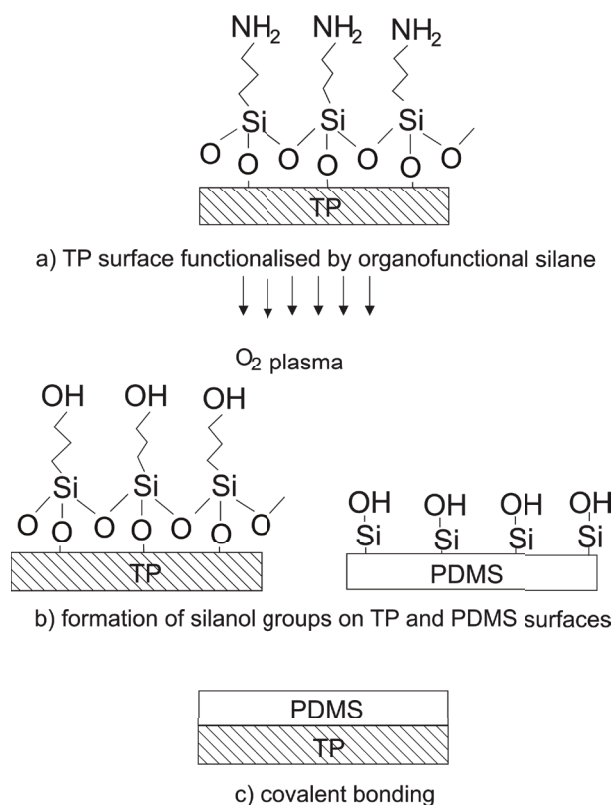


**Figure 2:** Process flow for TP-PDMS sandwich covalent bonding.

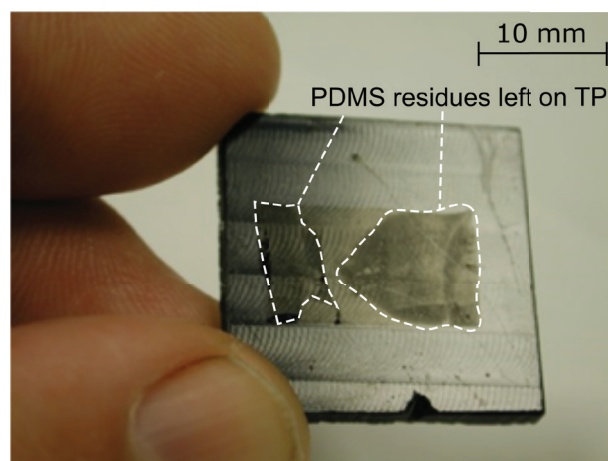


**Figure 3:** Photography of PDMS residues on ABS substrate after the PDMS elastomer was delaminated.

Next, the bond strengths were measured using burst pressure test devices. Top view and lateral cross-section of designed burst pressure test device is shown in Fig. 4.

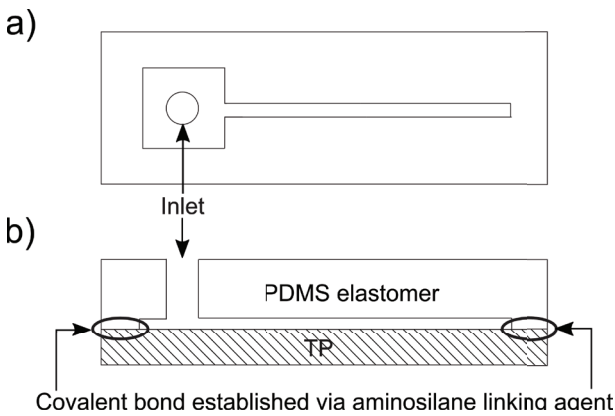


**Figure 4:** Schematics illustration of burst pressure test device. Top view (a) and lateral cross section (b).

Devices were fabricated by employing replica molding technique. Silicon mold for PDMS cast was fabricated by one-step photolithography and deep reactive ion etching (DRIE). Casted PDMS elastomer layers with microstructures (square-shaped inlet chambers with microchannels) were thermally cured at 60 °C for 1 hour and bonded to TP substrates applying bonding process described in Sect. 2.3.

Pressure regulated air supply was connected to the inlet of the test device and the pressure at which the device failed was determined. Device always failed at the region where the square-shaped inlet chamber narrows into the channel indicated by arrow position in Fig. 6. Here, the structural stress caused by applied fluidic pressure was the largest.

The region of failure was further confirmed by employing 3-D numerical simulations in COMSOL Multiphysics software. Test device behavior can be explained considering two different physics models coupled together. Fluid flow is described by the Navier-Stokes equation

$$\rho \frac{\partial \mathbf{v}}{\partial t} + \rho(\mathbf{v} \cdot \nabla)\mathbf{v} = \nabla \left[ -p\mathbf{I} + \mu \left( \nabla \mathbf{v} + (\nabla \mathbf{v})^T \right) \right] + \mathbf{F} \quad (1)$$

where the left hand side represents contribution of the force acting on a differential volume of a fluid and the inertial force.  $\mathbf{v}$  is the fluid velocity,  $\rho$  density,  $p$  pressure and  $\mu$  dynamic viscosity. Equation (1), which is describing conservation of momentum, needs to be solved together with equation of mass continuity which for incompressible fluid reads

$$\nabla \cdot \mathbf{v} = 0 \quad (2)$$

Deformation of a structure is modeled by structural mechanics equation for displacement vector  $\mathbf{u}$

$$\mathbf{f}_u = \rho \frac{\partial^2 \mathbf{u}}{\partial t^2} - \nabla \cdot \boldsymbol{\sigma} \quad (3)$$

where  $\mathbf{f}_u$  is a force acting on a differential volume and  $\boldsymbol{\sigma}$  is a stress tensor. Stress  $\boldsymbol{\sigma}$  and strain  $\boldsymbol{\varepsilon}$  tensors are related through equation  $\boldsymbol{\sigma} = \mathbf{c}_E \boldsymbol{\varepsilon}$ , where  $\mathbf{c}_E$  is the elasticity matrix (determined with Young modulus of elasticity and Poisson ratio). Equations (1) to (3) are solved for fluid velocities and structural deformations together with supporting relations described in the text. After the pressure boundary condition was applied on the inlet, stationary direct fully-coupled solver was employed to solve structural deformation and stress in burst pressure test device. Outlet boundary condition velocity was set to zero, although model tolerates also non-zero outlet boundary condition, due to coupled fluidic module. Simulated magnitude of bond stress at applied inlet fluidic pressure of 50 kPa is shown in Fig. 5. Maximum stress was calculated at the region (presented with dark red color in Fig. 5) where fabricated test devices failed first (pointed out with arrow in Fig. 6), which positively validated simulation model.

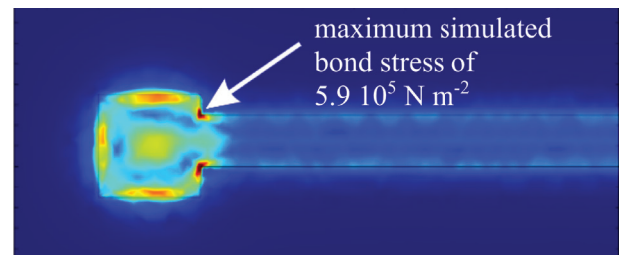


**Figure 5:** Simulated magnitude of bond stress at elevated fluidic pressure. Arrow indicates the point of maximum simulated bond stress.

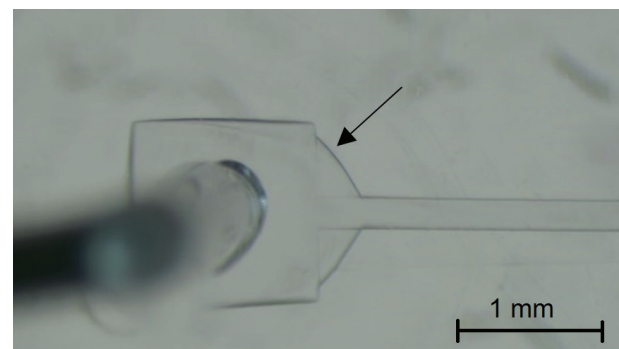


**Figure 6:** Micrograph of burst pressure test device. Arrow shows the failure onset region.

Simulation results show that the microfluidic channel design should avoid sharp edges throughout flow direction where layers delamination might be initiated.

### 3 Results

Since surfaces wettability is an essential criterion for inspecting the degree of surface activation in covalent bonding procedures, WCAs were measured first on raw and with O<sub>2</sub> plasma treated TP and PDMS surfaces. Results are presented in Table 1 (see also Fig. 1).

**Table 1:** WCAs for raw and oxygen plasma treated samples.

Polymer	raw	O2 plasma (1 min)	O2 plasma (5 min)
ABS	87	27	32
PC	74	38	37
PMMA	69	45	47
PDMS	87	4.5	/

Next, APTES (5%v/v in DI) was employed for functionalization of TP surfaces. With respect to others [2, 12] an additional post-deposition heat treatment and modified post-deposition plasma treatment were introduced in order to improve hydrolytic stability of covalent bonds. As expected, oxygen plasma treatment after modified APTES functionalization considerably improved surfaces wettability (see Table 2), which indicates high surface concentration of hydroxyl groups. However, wettability still declined considerably over time. In this study, no straightforward correlation between wettability of TP surfaces and TP-PDMS bond strength was found after the TP surfaces were functionalized.

**Table 2:** WCAs for APTES functionalized and oxygen plasma treated samples.

Polymer	APTES (5%v/v in DI)			Bond strength O2 plasma (20 sek)
	[°] 0 min	[°] after 30 min	[°] after 24 h	
ABS	9.5	38.7	74	accept.
PC	14.5	47	81	accept.
PMMA	12.3	36.5	83	accept.

In further investigation, 30 burst pressure tests employing water and compressed air were performed on fabricated PDMS test devices where TPs were previously functionalized with APTES or amine-PDMS linker. Again, no direct correlation between TP type (receiving equal surface preparation and bonding process) and bond strength was found. All test devices could sustain air pressures of 5 bars for at least 3 hours.

However, when burst pressure tests were performed by pressurized water, APTES devices started to fail immediately

after the fluidic pressure of 1 bar was applied with a channel edge delamination rate of 7.5 μm min<sup>-1</sup> in spite of additional post-deposition heat treatment and modification of post-deposition plasma treatment.

Similar hydrolysis of covalent bonds established via conventionally treated APTES was reported by Aran K et al. [12]. Results from testing bond strength under applied air pressure showed that the thermoplastics - PDMS bond was able to withstand more than 227.8 kPa, which was the maximum limit of their measuring equipment, without any sign of delamination. In further tests, the channels of the microdevices were filled with water and stored at room temperature for 72 h or the devices were filled and completely immersed in water for 72 h.

Surprisingly, the reported bonding strength for APTES coated membranes remained very strong (over 227.8 kPa) in devices stored at room temperature for 72 h with the device channels filled with water. However, complete immersion of the devices in water for an extended period of time weakened the membrane bonding strength for all of their tested bonding methods.

In another study, S. Kevin Lee et al. [2] reported bond failure and delamination of PDMS-APTES-TP sandwich structure after subjected to burst pressure test with water compressed above 15 psi.

An overview of silane is needed in order to understand the mechanisms for hydrolysis-induced bond failure. An organofunctional silane is a molecule comprising a silicon atom with at least one bond to carbon to enable organic functionality [6]. The inorganic side of the silane molecule consists of a silicon atom bound to alkoxy groups through Si—O—C linkages [2]. Hydrolytic instability of these bound alkoxy groups allows silanes to hydrolyze in the presence of water, converting the bound alkoxy groups to hydroxyl groups while liberating alcohol molecules. Any contact with water after bond formation will result in Si—O—C bond hydrolysis and ultimately bond failure [6, 13]. Furthermore, Si—O—C bonds have also been found to form directly between alkoxy groups such as methoxy and surface hydroxyl groups via alcoholysis [14]. Hydrolytic bond failure can occur at three locations in the bonding structure, at the thermoplastics-silane interface, at the PDMS-silane interface, and in the silane network itself [15]. While direct interface hydrolysis is unlikely due to the stability of the amide bond, any hydrophilic groups at the interface can act as nucleation sites for water condensation, allowing the silane network near the interface to be plasticized and weakened [16]. A similar process can occur at the PDMS-silane interface but with the possibility of hydrolysis directly at the inter-

face in addition to the weakening of the silane network [17]. For the silane network itself, high crosslink density can provide a major increase in resistance. However, networks formed by typical silanes, containing three silanol groups, tend to be cyclic, decreasing their resistance to dissolution [18]. Addressing failure mechanisms in all three locations is necessary to ensure hydrolytic stability [6,18].

In further investigation, burst pressure tests were performed on amine-PDMS linker test devices fabricated on PC, ABS and acrylic glass using pressurized water. Test devices withstood 2 bar water pressure for 3 hours without any delamination observed. Moreover, amine-PDMS linker devices were soaked in water for one week and successfully withstood all additional burst pressure tests. All tests confirmed hydrolytic stability of TP-PDMS bonds established through amine-PDMS linker. It is speculated that the water-repelling nature of the PDMS component in amine-PDMS linker prevented penetration of the aqueous solutions at the interface improving bond hydrolytic resistance [2, 3, 6].

Finally, developed bonding processes employing AP-TES and amine-PDMS linker were applied in modified micropump fabrication process. Based on the poor results of water tests on burst pressure devices, we further modified the APTES application by using multiple deposition steps (3 to 5 deposited layers), thus expecting the improvements of bonds hydrolytic resistance.

Our previously developed piezoelectric microcylinder pump prototypes [19] comprise activated PDMS elastomer layer bonded on its bottom side to the supporting bottom glass. Supporting bottom glass includes improvised fluidic connections and serves as a functional part of the micropump affecting micropump performance characteristics. Replacing supporting bottom glass with TP could pave the path toward micropump mass production in terms of enclosing the micropump in professional TP housing comprising professional fluidic and electric connections.

In the initial stage, supporting bottom glass was replaced with flat TP substrate. Exploded view of a typical TP microcylinder pump structure is shown in Fig. 7.

The TP microcylinder pump comprises PDMS elastomer layer with molded micropump chamber, fluidic microchannel and rectifying elements (Fig. 7 c). Additionally, two through-holes are punched into an elastomer, one into the center of the micropump chamber and the other one at the end of the channel. PDMS elastomer layer (Fig. 7 c) and PDMS fluidic connections (Fig. 7 e) are covalently bonded to the supporting TP substrate (Fig. 7 d) by employing developed multiple deposition

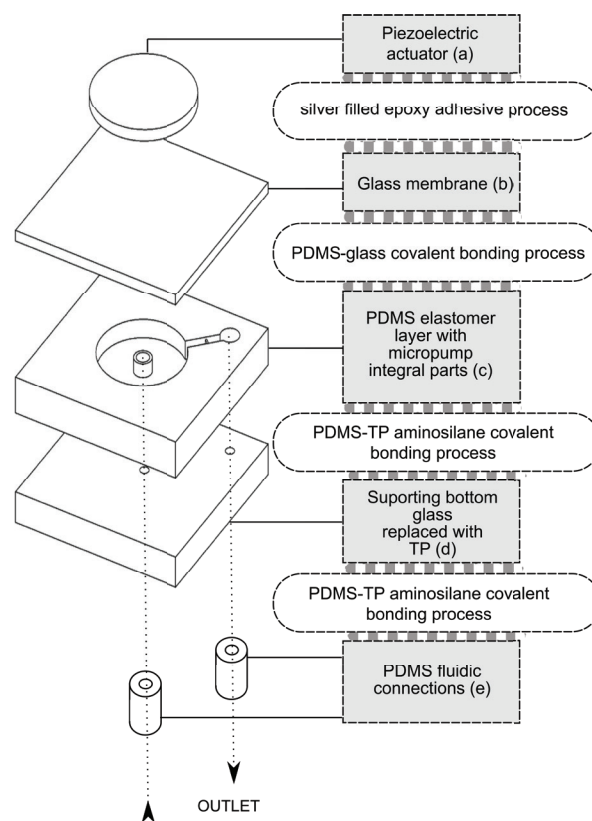


**Figure 7:** Exploded view of a typical TP microcylinder pump structure (dimensions are not to scale).

APTES or single deposition amine-PDMS linker bonding process.

One inlet and one outlet fluid port is drilled through a supporting TP substrate that supply and drain the fluid into and out of the pump. The micropump chamber and the microchannel are sealed with a thin glass membrane (Fig. 7 b) by employing oxygen plasma PDMS-glass covalent bonding process. Piezoelectric actuator (Fig 7 a) is positioned in the axis of a micropump chamber, coupled rigidly to the micropump membrane through silver filled epoxy adhesive (EPO-TEK EE129-4).

During excitation loosely attached glass membrane and PDMS elastomer layer deform in a controlled manner, which enables compression and expansion of the centrally placed inlet cylindrical port, micropump chamber and outlet throttle shaped port with a specific phase lag, contributing to efficient micropump operation.

Pumping test were performed by pumping air and DI water media. Both approaches passed air pumping tests, reaching maximum flow rate performance of 8 ml min<sup>-1</sup> and maximum backpressure performance of 100 mbar at applied square excitation waveform

with an amplitude of 140 V and a frequency of 300 Hz. However, during DI water pumping tests and despite improved multiple layer deposition process of APTES, micropumps degraded after several minutes of operation. This is depicted in Fig. 8 as APTES MP3 characteristics and further expanded on time scale in an in-set (see Fig. 8 central plot on the figure plane).

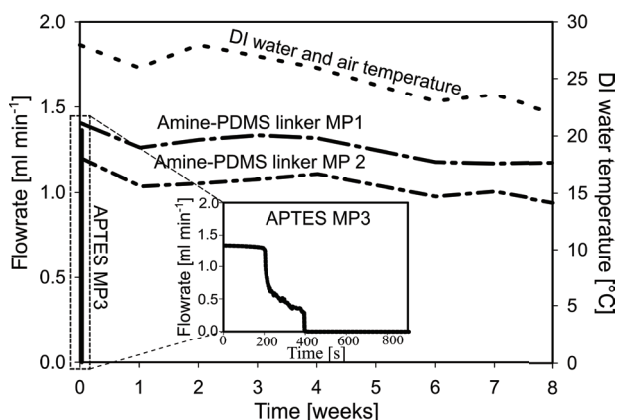


**Figure 8:** Long term flowrate stability characteristics of three representative micropump devices and ambient temperature.

In contrast, amine-PDMS linker composed of a PDMS backbone incorporating an amine side group established hydrolytically stable covalent bonds. This was confirmed by long-term flowrate stability measurements on two micropumps MP1 and MP2 with typical performances yielding initial maximum DI water flowrate performance of 1.2 ml min<sup>-1</sup> and 1.4 ml min<sup>-1</sup> at applied RC excitation waveform [20] with an amplitude of 140 V and a frequency of 300 Hz. Figure 8 also includes measurement setup ambient temperature (dotted line closest to the upper edge of the diagram). Due to partial correlation between flowrate performance characteristics of MP1 and MP2 and measurement setup ambient temperature it was concluded that transient deviations in flowrate characteristics are to be attributed to temperature changes of the medium viscosity, the micropump and driving electronics throughout the measurement. Therefore, long term stability measurements should be improved by setting measuring setup in a temperature stabilized chamber. Micropumps employing amine-PDMS linker bonding process exhibit no deterioration in their performance after eight weeks of continuous operation.

## 4 Conclusions

Low temperature process for TP-PDMS irreversible covalent bonding was presented. Process is based on silylation of the TP surfaces through the use of orga-

nonfunctional silanes. As the silanol groups are polar in nature, they make the exposed surface highly hydrophilic and this was observed by measuring WCAs. However in this study, no direct correlation between wettability of TP surfaces deposited with APTES and final bond strength was found. In further investigation, burst pressure tests were performed on designed and fabricated PDMS test devices employing TPs functionalized with APTES or amine-PDMS linker. All devices sustained air pressures of 5 bars for at least 3 hours, but only amine-PDMS linker test devices sustained continuous water pressure as high as 2 bars without delamination. Bonds established via APTES and subjected to water decayed in spite of additional post-deposition heat treatment and modification of post-deposition plasma treatment. In further application oriented study, both bonding processes were applied on piezoelectric micropumps where glass substrate was replaced by thermoplastic substrate. Even implementation of multiple deposition steps of APTES was insufficient in preventing hydrolysis of covalent bonds, resulting in micropumps performance deterioration. On the other hand, micropumps employing amine-PDMS linker exhibit no deterioration in their performance even after eight weeks of continuous operation.

## 5 Acknowledgments

Authors would like to thank the Slovenian Research Agency/ARRS (P2-0105, P2-0244), Ministry of Education, Science and Sport and Kolektor Group d.d. for their support of this work.

## 6 References

1. Yetisen, A. K., Akram, M. S., & Lowe, C. R. (2013). Based microfluidic point-of-care diagnostic devices. *Lab on a Chip*, 13(12), 2210-2251.
2. Lee, S. K., Lee, H., & Ram, J. R. (2016). U.S. Patent No. 9,422,409. Washington, DC: U.S. Patent and Trademark Office.
3. Wu, J., & Lee, N. Y. (2014). One-step surface modification for irreversible bonding of various plastics with a poly (dimethylsiloxane) elastomer at room temperature. *Lab on a Chip*, 14(9), 1564-1571.
4. Suzuki, Y., Yamada, M., & Seki, M. (2010). Sol-gel based fabrication of hybrid microfluidic devices composed of PDMS and thermoplastic substrates. *Sensors and Actuators B: Chemical*, 148(1), 323-329.
5. Tsao, C. W., & DeVoe, D. L. (2009). Bonding of thermoplastic polymer microfluidics. *Microfluidics and Nanofluidics*, 6(1), 1-16.

6. Lee, K. S., & Ram, R. J. (2009). Plastic–PDMS bonding for high pressure hydrolytically stable active microfluidics. *Lab on a Chip*, 9(11), 1618-1624.
7. Tang, L., & Lee, N. Y. (2010). A facile route for irreversible bonding of plastic-PDMS hybrid microdevices at room temperature. *Lab on a Chip*, 10(10), 1274-1280.
8. Karakoy, M., Gultepe, E., Pandey, S., Khashab, M. A., & Gracias, D. H. (2014). Silane surface modification for improved bioadhesion of esophageal stents. *Applied surface science*, 311, 684-689.
9. Garbassi, F., Morra, M., Occhiello, E., & Garbassi, F. (1998). *Polymer surfaces: from physics to technology* (pp. 169-200). Chichester: Wiley.
10. Hillborg, H., & Gedde, U. W. (1999). Hydrophobicity changes in silicone rubbers. *IEEE Transactions on Dielectrics and Electrical insulation*, 6(5), 703-717.
11. Bhattacharya, S., Datta, A., Berg, J. M., & Gangopadhyay, S. (2005). Studies on surface wettability of poly (dimethyl) siloxane (PDMS) and glass under oxygen-plasma treatment and correlation with bond strength. *Journal of microelectromechanical systems*, 14(3), 590-597.
12. Aran, K., Sasso, L. A., Kamdar, N., & Zahn, J. D. (2010). Irreversible, direct bonding of nanoporous polymer membranes to PDMS or glass microdevices. *Lab on a Chip*, 10(5), 548-552.
13. Goebel, R. (2003). U.S. Patent No. 6,613,439. Washington, DC: U.S. Patent and Trademark Office.
14. Pape, P. G., & Plueddemann, E. P. (1991). Methods for improving the performance of silane coupling agents. *Journal of adhesion science and technology*, 5(10), 831-842.
15. Plueddemann, E. P. (1991). Reminiscing on silane coupling agents. *Journal of Adhesion Science and Technology*, 5(4), 261-277.
16. Tesoro, G., & Wu, Y. (1991). Silane coupling agents: the role of the organofunctional group. *Journal of adhesion science and technology*, 5(10), 771-784.
17. Battjes, K. P., Barolo, A. M., & Dreyfuss, P. (1991). New evidence related to reactions of aminated silane coupling agents with carbon dioxide. *Journal of Adhesion Science and Technology*, 5(10), 785-799.
18. Plueddemann, E. P. (1991). Adhesion through silane coupling agents. In *Fundamentals of adhesion* (pp. 279-290). Springer US.
19. Dolžan, T., Pečar, B., Možek, M., Resnik, D., & Vrtačnik, D. (2015). Self-priming bubble tolerant microcylinder pump. *Sensors and Actuators A: Physical*, 233, 548-556.
20. [http://www.electronics-tutorials.ws/rc/rc\\_3.html](http://www.electronics-tutorials.ws/rc/rc_3.html) (17.10.2017)

Arrived: 31. 08. 2017

Accepted: 26. 10. 2017

# *Development and Evaluation of the Angular Response Measurement Setup for Solar Cells*

*Gašper Matič, Marko Jankovec, Marko Topič*

*University of Ljubljana, Faculty of Electrical Engineering, Ljubljana, Slovenia*

**Abstract:** The paper presents the development and practical evaluation of a basic setup for measuring the angular dependence of solar cells. The main goal of this study is to verify whether it is possible to use off-the-shelf components to build a simple but reliable measurement setup which performs fast and efficient characterization of angular dependence and therefore enables quick evaluation of various design ideas, especially when it comes to evaluating reference solar cells. The proposed setup consists of a rotary stage, a source measure unit for measuring the short circuit current of a cell under test, a digital multimeter for measuring the irradiance power drift via a photodiode, a solar simulator and a computer which controls all of the instruments. The paper focuses on the mechanical construction of the setup and on the problems affecting the measurement precision, to which appropriate solutions are proposed.

**Keywords:** solar cells, angular response, measurement setup development, mechanical construction, measurement precision issues

## *Razvoj in ovrednotenje sistema za merjenje kotne odvisnosti sončnih celic*

**Izvleček:** Sledeči članek predstavlja razvoj in praktično ovrednotenje osnovnega sistema za merjenje kotne odvisnosti sončnih celic. Poglavitni namen študije je preveriti, ali je mogoče s pomočjo splošno dostopnih komponent izdelati enostaven vendar zanesljiv merilni sistem, ki nudi hitro in učinkovito karakterizacijo kotne odvisnosti ter tako omogoča nezamudno ovrednotenje različnih načrtovalskih idej, še posebej v primeru ovrednotenja referenčnih sončnih celic. Predlagani merilni sistem sestoji iz rotacijske enote, napajalno-merilne enote za merjenje kratkostičnega toka merjene sončne celice, digitalnega multimetra za merjenje lezenja jakosti osvetlitve s pomočjo fotodiode, simulatorja sončnega obsevanja in računalnika, ki nadzoruje vse inštrumente. Članek se osredotoča na izvedbo mehanske konstrukcije merilnega sistema ter na težave povezane z merilno točnostjo in natančnostjo, za katere predlagamo ustrezne rešitve.

**Ključne besede:** sončne celice, kotna odvisnost, razvoj merilnega sistema, mehanska konstrukcija, merilna točnost in natančnost

\* Corresponding Author's e-mail: [gasper.matic@fe.uni-lj.si](mailto:gasper.matic@fe.uni-lj.si)

### *1 Introduction*

Angular response of a photovoltaic module plays an important role since it is related to angle-dependent energy losses [1], which can become a crucial part of yearly performance losses due to nonstandard operating conditions [2] or due to poor orientations and tilt angles [1]. An accurate knowledge of the angular dependence is also important in predicting the performance of a PV system [2] and crucial to the precision of photovoltaic sensors [3]. All of the above makes the angular response measurement setup an essential part of the PV characterization equipment. Although many studies and experiments have been published concerning the behavior of the angular response of solar

cells (e.g. [2], [1], [3]), there is usually little specific detail on constructing the actual angular response measurement setup and on the problems related with performing accurate measurements.

In this paper we present the development and practical evaluation of a basic setup for measuring the angular dependence of solar cells. The focus is put on the mechanical construction of the setup and on the problems that arise during measurements and affect the measurement precision.

## 2 Setup construction

### 2.1 Setup description

The setup is basically comprised of a Keithley 238 SMU source measure unit which is used to provide 4-wire measurements of the short circuit current of the device under test (DUT); an Agilent A34401A digital multimeter used for measuring the irradiance power drift via a reference photodiode; a Newport Oriel Class A solar simulator 93194A; a precision rotary stage OWIS DMT65 used to set the DUT's angle of incidence and a computer which controls all of the instruments via a Labview routine through GPIB (General Purpose Interface Bus) and USB interfaces. At this point of development we are interested in using such a setup only to precisely measure the shape of the angular response and to be able to make relative comparisons of responses from different solar cells, which is why the measured responses presented in the paper are typically normalized and represented by the abbreviation NR (i.e. normalized response).

### 2.2 Mechanical construction

The supporting construction for the DMT65 rotary stage (Figure 1 and Figure 2) was built from a medium-density fiberboard (MDF) because this material is consistent in strength and size, has stable dimensions (in normal environmental conditions it does not expand or twist like wood, especially if painted) and is easy to shape. The rotary stage was mounted so that the axis of rotation becomes horizontal. The stage was placed on a spacer which allows a 20 cm long rail (Edmund optics) to be fixed onto it. The rail allows the distance between the DUT and the line of the rotation axis to be set. Two dovetail slide carriers were then attached onto the rail. These slide carriers hold the right angle metal bracket, onto which the optical filter holder (Edmund optics) is then fixed. The filter holder is used to hold the DUT in place during the rotation. Typically, devices under test were attached to a special Plexiglas adapter which was then inserted into the filter holder. The mounting of the rotary stage onto the supporting construction was reinforced in order to minimize the bending when the DUT is inserted into the holder. The rigidity and mechanical stability of the whole setup is crucial for good repeatability and comparison of the measurements. Almost every construction part was spray painted with black matte paint in order to minimize light reflections. The rotary stage was mounted onto a tabletop that was placed on two supporting columns of modular spacers, which allow the distance between the DUT and the solar simulator lens to be varied (Figure 1).



**Figure 1:** The rotary stage mounted onto the supporting construction. A DUT is mounted into a Plexiglas adapter which is then attached to the rotary stage through the two-screw optical filter holder.

## 3 Measurement precision issues

In the following, four groups of problems which, in our opinion, have important effect on measurement precision are discussed.

### 3.1 Mechanical and geometrical problems

#### 3.1.1 Mounting the DUT into the setup

Firstly, it must be assured that the distance between the DUT's photosensitive area and the imaginary line of the rotation axis is as small as possible. Secondly, this imaginary line must also run so that it splits the photosensitive area into two symmetrical parts. When these two conditions are met, the average distance between the photosensitive area and the source of (imperfectly) collimated light (i.e. the solar simulator collimating lens) does not change during the rotation. If it would, this would be a source of a systematic measurement error because at some point the photosensitive area would be in average closer to the source of light than at some other point.

While the second problem of aligning the line of symmetry of the photosensitive area with the line of the rotation axis is simply a matter of proper positioning of the DUT when inserting it into the holder, the first problem of minimizing the distance between the photosensitive area and the line of the rotation axis requires ad-

ditional calibration. A simple solution is possible using a laser-cut Plexiglas calibration tool (Figure 2). The calibration procedure is as follows. First, additional slide carrier is attached onto the rail so that its top face lies exactly at the axis of rotation (Figure 3). This is how we get a zero-height reference point on the rail. Then an optional spacer is put on top of this carrier, which compensates for the material that covers the photosensitive area (in our example this is glass and ethylene-vinyl acetate (EVA) laminate). At the top of this spacer comes the bottom of the calibration tool. At the same time the vertical side of the calibration tool is pressed parallel to the rail. Now the two slide carriers that attach the DUT to the rail are made loose which allows the DUT to be slid upwards to meet the horizontal side of the calibration tool (Figure 2). Since the horizontal side of the calibration tool is perpendicular to the vertical side, the height relative to the rotation axis at the bottom of the tool is now the same as at the horizontal side that is touching the top of the DUT (i.e. the glass in our case – see Figure 2). In other words, the calibration tool simply helps translate the level at its bottom over the mechanical parts that hold the DUT to the location where the DUT actually lies.

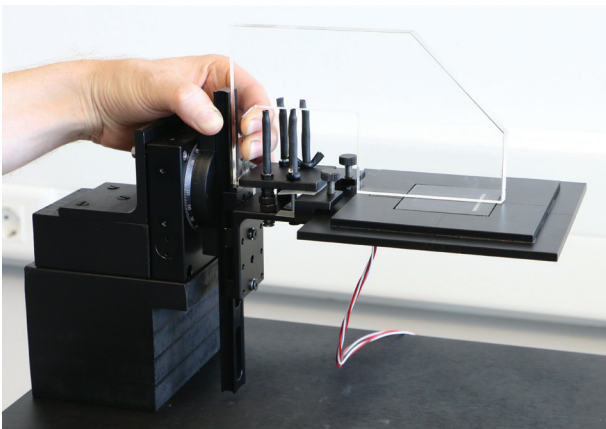


**Figure 2:** Calibrating the distance between the photosensitive area of the DUT and the imaginary line of the rotation axis. At the same time the tilt of the DUT relative to the holder can be minimized.

The height of the DUT on the rail is now set so that the photosensitive area that lies beneath the glass and EVA laminate is at the same height as the imaginary line of the rotation axis. The optional spacer assures that the DUT is moved slightly higher, compensating for the thickness of glass and EVA. As a matter of interest, some setups do not perform this compensation (e.g. [1]).

Typically, it is desired that the plane of the photosensitive area is parallel to the line of the rotation axis. The calibration tool can also be used to minimize the tilt of the DUT. A narrow strip of elastic material is placed

between a Plexiglas DUT adapter and the filter holder. If this strip is placed at the right location, then we can control the tilt of the DUT by increasing or decreasing the force provided by the two fastening screws in the filter holder. The elastic strip contracts under the pressure which causes the DUT adapter to tilt upwards or downwards, depending on the location of the strip relative to the screws. The tilt of the DUT is minimized when the face of the DUT is parallel to the horizontal side of the calibration tool (Figure 2). But in some situations it is useful to provide a small amount of tilt as we will demonstrate later.

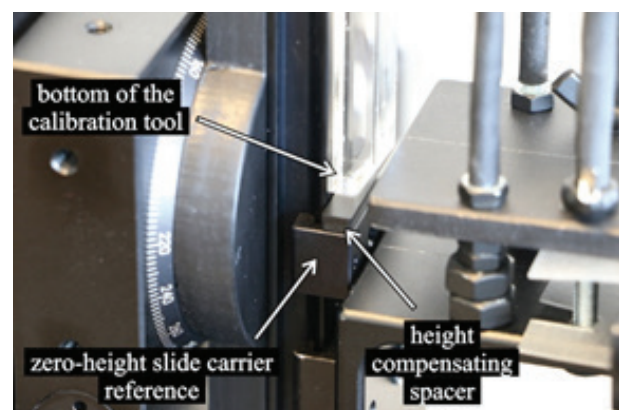


**Figure 3:** Calibrating the distance between the photosensitive area of the DUT and the imaginary line of the rotation axis – a detail.

### 3.1.2 Initial position problem

When the DUT is fixed into the setup, the measurements can begin. But in order to provide measurements with high repeatability which can be used in quality comparison analyses, the *same* initial position for all measurements must be defined. In order to demonstrate the importance in the precision and repeatability of the initial point, let us study the plot in Figure 4. The plot shows a comparison of a short circuit current response for two similar reference cells: one with white back sheet and the other with black back sheet. From the short circuit current ratio (solid line) one would conclude that the first cell has better response at high angles of incidence  $\alpha$  than the second cell. Now, if the initial point of the measurement for the second DUT is offset by  $1^\circ$  relative to the original initial point (dashed line), a completely different conclusion is derived. The angular response measurements are very sensitive to errors in mechanical positioning, especially at high angles [4] due to the increased slope of the response.

The initial position problem is not as simple as it seems at first sight. For instance, if we decide to use a fixed absolute position of our rotary stage as the initial point, then as soon as the setup (or DUT) is moved from its current location, the actual orientation of the setup

(and DUT) relative to the beam of light emanating from the solar simulator may change. This means that the irradiance at the initial point becomes sensitive to the orientation and position of the setup (and DUT), which is a nuisance if precise measurements with high repeatability are required. Besides, the precision and repeatability of the absolute home reference point of the rotary stage may also be problematic, as it proved in our case.

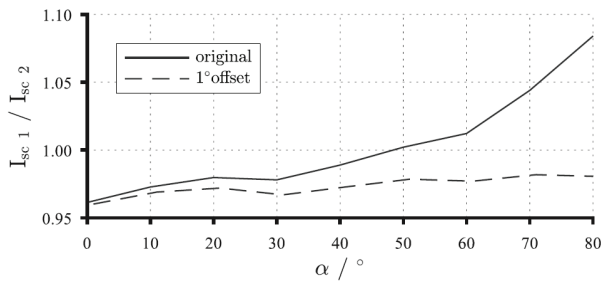


**Figure 4:** The effect of the precision of the initial point of a measurement. A relatively small offset in the initial point position can cause a completely different measurement conclusion when comparing short circuit responses of two different solar cells.

From the thought experiment above one can already sense the solution to this problem. The initial point must be defined relative to the beam of light provided by the solar simulator. If before each measurement the rotary stage is positioned so that the light hits the DUT at zero angle of incidence, i.e.  $\alpha = 0^\circ \equiv \alpha_0$ , then the repeatability of the measurement results is very much improved and does not depend on the exactness of the position and orientation of the setup and DUT.

The process of finding the position of the rotary stage where the zero angle of incidence occurs at DUT can be automated in our measurement setup. We developed two algorithms to calibrate the  $\alpha_0$  point. The first algorithm is based on a fact that at the zero angle of incidence a DUT provides the maximal response. The algorithm is therefore designed to iteratively search for the maximal response in a given range of rotational positions by sampling the DUT response with a specified resolution. At each next iteration, the range is narrowed and the resolution increased. The algorithm stops at the prescribed minimal resolution and the point of maximal response is declared the zero incidence angle  $\alpha_0$ . In order to decrease the effect of the measurement noise, the measurement samples can be smoothed by filtering and the algorithm then works with the smoothed samples. The problem with this approach is that the typical response of a DUT has the shape of a cosine function [1], which means that the maximum is very unpronounced, i.e. the small region around the peak is very flat, which makes the detection

of the peak location difficult and at the same time the effect of measurement noise is increased. Nevertheless, the algorithm has still proved useful in most cases, especially if averaging of the measurement samples is increased.

The second algorithm we devised takes into account the problem of the unpronounced maximum and searches for the  $\alpha_0$  point indirectly. The algorithm is based on a fact that in most cases the angular response of a solar cell is very much symmetrical [1] in a region near the  $\alpha_0$  point. Therefore, the  $\alpha_0$  point is determined on a criterion that for symmetrical angles  $\pm\alpha$  around the  $\alpha_0$  point the measurement samples have the maximal symmetry. The idea is demonstrated in Figure 5. Three measurement sets are made with samples 15° apart. Each next measurement set is offset by  $\Delta\alpha$  from the previous set. The central measurement samples of each set lie around the actual zero angle of incidence point  $\alpha = 0 = \alpha_0$ . Now for each of the sets the symmetry around the central sample is checked. For the first set we can observe that samples left of the central point (negative  $\alpha$ ) have smaller measured values than their symmetrical counterparts on the right side of the central point (positive  $\alpha$ ).

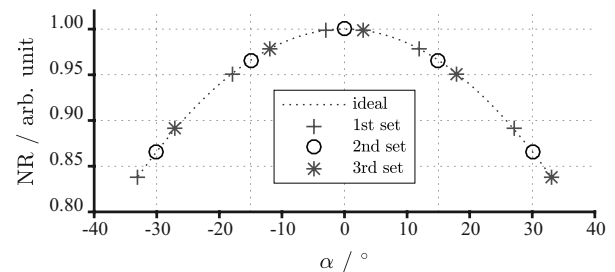


**Figure 5:** Calibrating the zero angle of incidence point  $\alpha_0$  by maximizing the symmetry of the samples around the  $\alpha_0$  point.

Obviously, there is an asymmetry to this set and we can conclude that the central point of the set does not lie in the zero angle of incidence point. Similar is true for the third measurement set, where the situation is turned around. In case of the second measurement set, at symmetrical angles around the central point we get symmetrical measurement samples, which indicates that the central point of the second set lies in the  $\alpha_0$  point. The zero incidence angle is thus determined indirectly via the symmetry criterion. The algorithm proved to be much more sensitive with a much more pronounced maximum of the criterion function, which results in a high repeatability of the calibration results. The resolution of this search algorithm is determined by the offset between the sequential measurement sets  $\Delta\alpha$ . In our experience, the  $\Delta\alpha = 0,2^\circ$  proved to be a practical value for the offset.

We performed a repeatability test for the second algorithm in the following way: a reference solar cell was mounted into the setup and then the calibration algorithm was run 15 times. The absolute position of the rotary stage (i.e. the absolute offset of the stage) where the  $\alpha_0$  point was detected was then recorded and used to plot a histogram in Figure 6. Obviously, the repeatability of the zero angle of incidence point is quite high, especially if the averaging of the measurement samples is increased.

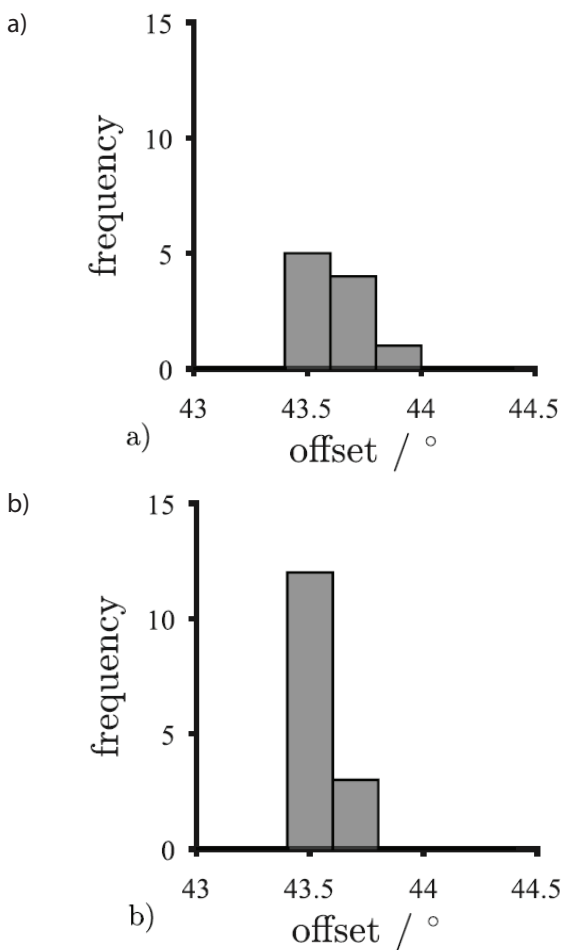


**Figure 6:** A repeatability test for the calibration of the zero angle of incidence point  $\alpha_0$ . In case of b), the averaging of the measurement samples was increased. The resolution of the calibration was  $\Delta\alpha = 0,2^\circ$ .

The obvious drawback of the second algorithm is that it can be used only in cases where the expected response is fairly symmetrical. Luckily, this practically holds true in many cases. In cases of asymmetrical responses, the first algorithm can be used instead or both algorithms combined, using the second algorithm only on a smaller region that still displays fair symmetry.

### 3.2 Optical problems

The first problem that can be considered as an optical one is the problem of stray light. By stray light we mean the light that emanates from the solar simulator and reaches the DUT indirectly due to reflections from the surrounding objects. Minimizing stray light is important since it can cause large relative measurement errors at higher angles of incidence. Namely, at very high angles there is expected that less and less direct excitation light reaches the photosensitive area (at  $90^\circ$  no light should hit the area), so the DUT response should approach zero value. But if the stray light is present and hits the DUT, this is not the case since the stray light cannot be distinguished from the direct excitation light and its effect compensated from the measurements. In order to minimize this effect, we developed a cascade system of masks that are placed in between the solar simulator lens and a DUT with intention to shape the light beam only to the DUT and the nearby surrounding area (Figure 7). Also, the objects surrounding the setup were either moved far away or covered with a low reflectance mask (i.e. black painted plywood).

The second problem also deals with indirect light hitting the photosensitive area, but in this case the light is not reflected from the surrounding objects but from the solar simulator optics itself. These reflections are named multiple- or also double-reflections and have been studied to some degree [5, 6].



**Figure 7:** A cascade system of masks that limit the light beam in order to minimize the stray light errors.

Most references claim that the light is reflected back to the DUT from the collimating lens, but we have

discovered that this is not a complete understanding of the problem. Namely, not just a lens, but every optical component that lies behind the lens inside the solar simulator also plays an important role in these double-reflections. These reflections cause a strong increase in DUT response near zero angle of incidence where a DUT reflects the incidence light directly back to the solar simulator. Figure 8 shows an example of this phenomenon in case of a WPVS reference cell from Fraunhofer ISE (see Figure 11a). The loss function is determined as a difference between the ideal normalized cosine response and the normalized measured value at a given angle  $\alpha$ .

To mitigate this problem, two different approaches were used. The first solution tilts the DUT in order to direct the light reflected from the DUT away from the central axis of the collimating lens (Figure 10a) thus redirecting these reflections away from the simulator optics. A tilt of e.g.  $\beta = 5^\circ$  causes a decrease in response at zero angle of incidence  $\alpha_0$  for a factor of  $\cos(5^\circ) = 0,9962$ , which is about 5 per mills. This factor can be simply neglected if only normalized measurement response is required. Figure 9 shows the mitigating effect of such a solution in case of the same WPVS reference cell.

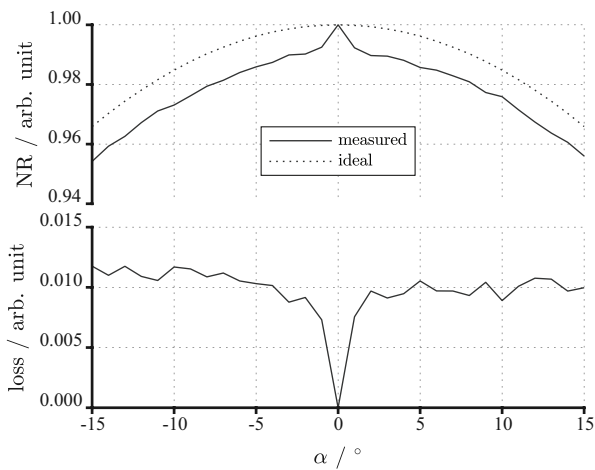


**Figure 8:** The effect of double-reflections in a measurement response of a WPVS reference cell. A relatively large spike occurs at zero angle of incidence.

The second solution (Figure 10b) moves the DUT away from the central line of the lens where double-reflections are most prominent and also increases the distance from the lens, which decreases the solid angle taken by the area of DUT as seen from the center of lens and therefore decreases the power density of double-reflected light. Besides, increasing the distance is also beneficial because it mitigates the effects of light beam uniformity [1]. The second solution is as effective as the first one and the solutions can, of course, be combined if needed.

To complete the picture about light hitting the DUT during measurements, we must explain how to deal with the effect of room ambient light. The procedure also applies to the case where a bias light is used to decrease the effect of non-linearity of a DUT at low illumination (as in e.g. [2]). Effect of this light can be easily compensated for in the following manner: at each angular position  $\alpha$  the response of the DUT is first measured *before* the DUT is exposed to the solar simulator light. In this way we get the information about the ambient light intensity. Then the electronic-controlled shutter is opened and another measurement is taken, combining the response to both ambient and solar simulator light. The final measurement result is simply the difference between the second and the first measurement, since it can be assumed that the DUT provides a linear response [1]. In this case it is important that the instrument that is measuring the response has the resolution that is high enough, since we are subtracting two measurements that can be close to each other. This compensation is actually a simple variant of a lock-in measurement technique.

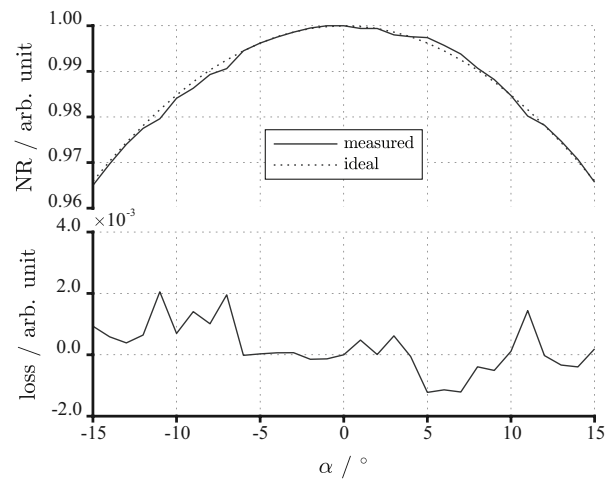


**Figure 9:** The effect of double-reflections in the case of a WPVS reference cell is mitigated by tilting the DUT.

The last problem concerning the optical circumstances is the problem of the solar simulator irradiance drift. This effect is compensated in the following way. At the same time when the DUT response is measured, the response of a reference PIN photodiode which measures the solar simulator irradiance intensity is also recorded. These reference irradiance measurements are then used to correct the DUT response measurements by scaling them all to the same irradiance intensity, relying on the proportionality of both DUT and PIN diode responses.

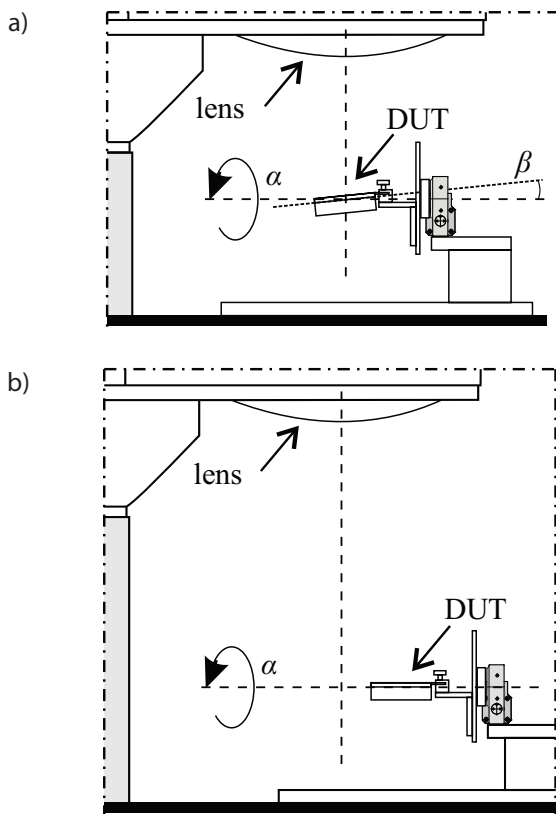


**Figure 10:** Two practical solutions to the double-reflections problem.

### 3.3 Temperature dependence

The main problem here is the rise of the DUT temperature due to the irradiation caused by the solar simulator, which affects the response of the DUT. Since our setup does not provide any kind of cooling mechanism as in [2] and since there are cases where the additional DUT temperature measurement for the temperature effect compensation is not available, the temperature problem can be addressed only by minimizing the temperature rise during the measurement. The *average* power absorbed by the DUT through irradiance  $\bar{P}$  is

$$\bar{P} = \frac{t_{ON}}{t_{ON} + t_{OFF}} P, \quad (1)$$

where  $P$  is the power being absorbed by the DUT when exposed to solar simulator light and the  $t_{ON}$  and  $t_{OFF}$  are the durations of the solar simulator shutter being opened and closed, respectively. Obviously, there are two ways in decreasing the average absorbed power  $\bar{P}$  during measurement and thus decreasing the temperature rise: the power of the solar simulator can be decreased, which decreases the  $P$  term, or the duty cycle of the shutter can be decreased by increasing the  $t_{OFF}$  term. The first solution can be easily achieved by

decreasing the power of the solar simulator lamp or increasing the distance between the DUT and the collimating lens, which at the same time helps mitigate the problem of double-reflections (see chapter 3.2). The second solution means that the time required to perform the whole measurement gets increased, which is not that problematic.

### 3.4 Electrical measurements

To increase the precision of the short circuit current measurements, a 4-wire measuring technique is used. As with any other precise electronic measurement, the important source of error is the measurement noise. Since in our case we are measuring a DC signal (i.e. a constant value response), the noise can be reduced by applying the averaging technique where greater number of measurement samples is taken and then averaged. But this means that the time when the DUT is exposed to the solar simulator light  $t_{ON}$  is also increased, which causes the DUT to heat up. In order to prevent this, the duty cycle of the shutter must not be changed. Instead the number of measurement samples for a given angle  $\alpha$  is increased using the same duty cycle. In other words, instead of making one long measurement with large  $t_{ON}$  we make several short measurements with small  $t_{ON}$  and unchanged shutter duty cycle, which means that the average absorbed power by the DUT is not increased. As an additional benefit of such an averaging several measurements for each angle  $\alpha$  are recorded, which means that the measurement uncertainty can be evaluated for each angle.

## 4 A measurement example

Angular responses of a reference cell that we developed were measured at three different stages of production: before lamination (i.e. bare), after lamination (glass and EVA on top) and when in enclosure (Figure 11 b), c) and d), respectively). The results are shown in Figure 12.

It can be clearly observed that the lamination reduces the losses at lower angles of incidence  $\alpha$ , while the losses at higher  $\alpha$  are increased, most probably due to the increased light reflection from the glass and due to different surface texturing [1]. The loss function of the laminated cell agrees well with the ones measured in [1]. The effect of the enclosure can also be observed, where at angles higher than about  $50^\circ$  the loss is increased due to the shading effect of the enclosure.

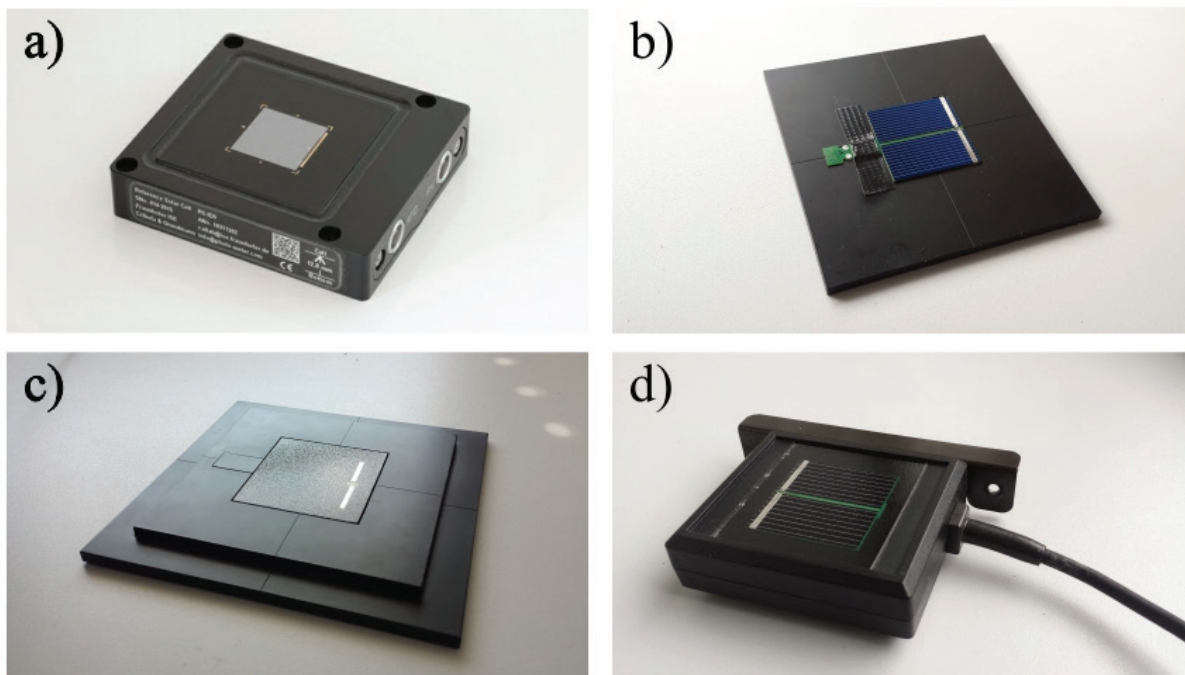


**Figure 11:** Devices under test: a) WPVS reference cell from Fraunhofer ISE and in-house developed mono-Si reference cells: b) non-laminated (bare), c) laminated (glass +EVA on top) and d) in-enclosure.

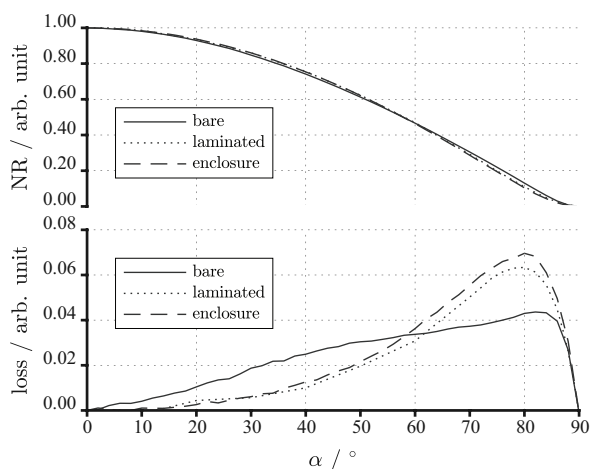


**Figure 12:** Normalized angular response of a mono-Si reference cell in three different stages of production.

## 5 Conclusion

A development of a basic setup for measuring the angular dependence of solar cells was presented. We believe that the concept of the proposed measurement setup proved successful as well as the solutions to the key problems that affect the measurement precision. The setup was used to perform a series of other measurement experiments which cannot be presented here and, to our belief, the setup proved precise with high level of repeatability being able to provide insightful

results, despite its somewhat simplistic approach. In future we are planning to validate the precision of our setup by comparing our results to the results of a certified measurement laboratory.

## 6 Acknowledgement

We would like to thank Mizarstvo Jankovec for kindly providing the wooden building blocks required for the setup construction.

## 7 References

1. J. L. Balenzategui and F. Chenlo, "Measurement and analysis of angular response of bare and encapsulated silicon solar cells," *Sol. Energy Mater. Sol. Cells*, vol. 86, no. 1, pp. 53–83, 2005.
2. I. Geisemeyer et al., "Angle dependence of solar cells and modules: The role of cell texturization," *IEEE J. Photovoltaics*, vol. 7, no. 1, pp. 19–24, 2017.
3. J. J. Michalsky, L. C. Harrison, and W. E. Berkheiser, "Cosine response characteristics of some radiometric and photometric sensors," *Sol. energy*, vol. 54, no. 6, pp. 397–402, 1995.
4. King, Boyson, Hansen, and Bower, "Improved Low-Cost Solar Irradiance Sensors," Albuquerque, New Mexico, 1998.

5. S. K. K. Morita, S. Kera, P. Sochor, "Solutions for Performance Measurement Error Due to Multiple-Reflections between Reference Solar Cell and Output Lens of Solar Simulator," in *27th European Photovoltaic Solar Energy Conference and Exhibition*, 2012, pp. 3693–3696.
6. U. K. D. Romang, J. Meier, R. Adelhelm, "Reference Solar Cell Reflections in Solar Simulators," in *26th European Photovoltaic Solar Energy Conference and Exhibition*, 2011, pp. 2613–2617.

Arrived: 31. 08. 2017

Accepted: 27. 10. 2017



# Multicaloric effect in polycrystalline $Pb(Fe_{0.5}Nb_{0.5})O_3$

Uros Prah<sup>1,2</sup>, Magdalena Wencka<sup>3</sup>, Zdravko Kutnjak<sup>1,2</sup>, Marko Vrabelj<sup>1</sup>, Silvo Drnovsek<sup>1</sup>,  
 Barbara Malic<sup>1,2</sup> and Hana Ursic<sup>1,2</sup>

<sup>1</sup>Jožef Stefan Institute, Ljubljana, Slovenia

<sup>2</sup>Jožef Stefan International Postgraduate School, Ljubljana, Slovenia

<sup>3</sup>Institute of Molecular Physics, Polish Academy of Sciences, Poznań, Poland

**Abstract:** In this work, magnetocaloric and electrocaloric properties of multiferroic  $Pb(Fe_{0.5}Nb_{0.5})O_3$  ceramics have been investigated.  $Pb(Fe_{0.5}Nb_{0.5})O_3$  was prepared by mechanochemical activation of constituent oxides, followed by sintering at 1273 K in oxygen atmosphere. Microstructure and X-ray powder-diffraction analysis revealed dense, homogeneous and uniform microstructure without the presence of undesired secondary phases. Magnetocaloric and electrocaloric effects were determined by the indirect methods - calculated from the changes of sample's magnetization and polarization, respectively. The maximal magnetocaloric temperature change (0.16 K at 50 kOe) was obtained at 2 K coinciding with the observed anomaly in magnetization vs. temperature measurement. On the other hand, at room temperature the pronounced electrocaloric effect was determined, namely 0.81 K at 80 kV/cm, while the maximal value of electrocaloric temperature change 1.29 K was obtained near the paraelectric-ferroelectric phase transition i.e., at 373 K.

**Keywords:** multiferroic; PFN; multicaloric; electrocaloric; magnetocaloric

## Multikalorični pojav v polikristaliničnem $Pb(Fe_{0.5}Nb_{0.5})O_3$

**Izveček:** V članku smo proučevali magnetokalorični in elektrokalorični pojav v multiferroičnem  $Pb(Fe_{0.5}Nb_{0.5})O_3$ . Keramiko smo pripravili z mehanokemijsko aktivacijo kovinskih oksidov, ki ji je sledilo sintranje pri 1273 K v kisikovi atmosferi. Mikrostruktura keramike je bila gosta in homogena. Sekundarnih faz nismo opazili. Tako magnetokalorično kot tudi elektrokalorično temperaturno spremembo smo izračunali iz temperaturne spremembe magnetizacije oz. polarizacije vzorca pri različnih zunanjih poljih. Največjo magnetokalorično spremembo temperature (0,16 K pri 50 kOe) smo določili pri 2 K, kar je v skladu z opaženo anomalijo magnetizacije vzorca v odvisnosti od temperature. Izrazito elektrokalorično spremembo temperature smo opazili že pri sobni temperaturi (0,81 K pri 80 kV/cm), medtem ko je bila njena maksimalna vrednost 1,29 K opažena v bližini paraelektričnega-feroelektričnega faznega prehoda pri 373 K.

**Ključne besede:** multiferroik; PFN; multikalorik; elektrokalorik; magnetokalorik

\*Corresponding Author's e-mail: uros.prah@ijs.si

### 1 Introduction

Nowadays the majority of commercially used refrigeration systems are still based on vapor-compression refrigeration cycle. This technology was discovered at the beginning of the 19<sup>th</sup> century and has been developed and perfected through the years. Despite all the improvements, the method shows a number of disadvantages. The major problems are low energy efficiency and the use of environmentally hazardous refrigerant media [1, 2]. These disadvantages has driven the development of more efficient and environmentally friendly cooling devices.

Solid-state refrigeration technology represents a promising alternative for the replacement of the conventional refrigeration systems. Most current activity in cooling research is looking at one of the caloric effects – magnetocaloric (MC), electrocaloric (EC) or mechano-caloric – where the material's entropy changes under the application of external stimuli –magnetic, electric, or mechanical (stress) [3]. However, in bulk ceramic materials the caloric effect is currently not large enough for commercial use. One idea how to overcome this problem is to prepare a material exhibiting more than one caloric effect, called multicaloric material, in which

the application of two or more stimuli can enhance the total caloric effect. Further, different caloric modes can be applied in different temperature regions extending the operating temperature range of the cooling device [4].

In 2012, the coexistence of the MC and EC effects in a single-phase material was theoretically introduced for the first time [5]. In the next years, many theoretical reports were followed [6-8]. In 2014, a multicaloric effect in  $Y_2CoMnO_6$  was experimentally observed [9]. However, this material exhibit improper multiferroic properties and therefore the conventional methods for determining the EC effect are not appropriate. In 2016 the existence of multicaloric properties in  $0.8Pb(Fe_{0.5}Nb_{0.5})O_3-0.2Pb(Mg_{0.5}W_{0.5})O_3$  (PFN-20PMW) ceramic material was demonstrated, where the coexistence of MC and EC effects was unequivocally experimentally confirmed [4]. While PFN-20PMW appears promising, it possesses very small MC and EC temperature changes (both  $\sim 0.25$  K). Further, the largest caloric effects in this material are observed at low temperatures of 5 K (MC) and 220 K (EC), which is far too low for any practical applications.

One of the more promising candidates is multiferroic  $Pb(Fe_{0.5}Nb_{0.5})O_3$  (PFN) ceramic. It possesses a relatively high peak of the dielectric permittivity (several 10,000) at around 370 K, which is attributed to the paraelectric-ferroelectric phase transition [10]. Because the highest caloric effects are obtained near ferroic phase transitions [11, 12], PFN should possess high EC properties above the room temperature. On the other hand, in this material two anomalies are reported also in the temperature dependence of the magnetic susceptibility. These two anomalies appear at 150 K and 10 K [13, 14] indicating a potential for enhanced MC effect close to these temperatures.

One possibility of preparing complex oxides is the use of mechanochemical synthesis, where homogeneous powders can be prepared without thermal treatment. Later the powder compacts are sintered at elevated temperature ( $T > 1200$  K) to obtain dense ceramics. It was shown that  $(K_{0.485}Na_{0.485}Li_{0.03})(Nb_{0.8}Ta_{0.2})O_3$  and  $Pb(Sc_{0.5}Nb_{0.5})O_3$  ceramics prepared from the mechanochemically synthesized powders have exhibited superior chemical homogeneity in comparison to the one prepared by the classical solid-state synthesis [15, 16]. PFN has already been prepared with a mechanochemical synthesis [17-19] and in comparison to the solid-state synthesized samples, it possesses higher values of peak-permittivity, which can be presumably attributed to the better chemical homogeneity of the former one [15]. In this work we prepared a single-phase PFN ceramic by mechanochemical synthesis and sintering

aiming to study its dielectric, electrocaloric and magnetocaloric properties.

## 2 Experimental

For the synthesis of the PFN powder,  $Nb_2O_5$  (99.9%, Sigma-Aldrich, 208515),  $Fe_2O_3$  (99.9%, Alfa, 014680-Ventron) and  $PbO$  (99.9%, Sigma-Aldrich, 211907) were used. The homogenized stoichiometric mixture (200 g) was mechanochemically activated in a high-energy planetary ball mill (Retsch, Model PM 400) for 30 h at 300 rpm using a tungsten carbide milling vial ( $250\text{ cm}^3$ ) and 15 balls ( $2r = 20$  mm). The synthesized powder was milled in an attrition mill with yttria-stabilized zirconia balls ( $2r = 3$  mm) in isopropanol, for 4 h at 800 rpm.

The powder was then uniaxially pressed (50 MPa) into pellets and further consolidated by isostatic pressing at 300 MPa. The powder compacts were sintered in double alumina crucibles in the presence of a packing powder with the same chemical composition, in order to avoid possible  $PbO$  losses. The compacts were sintered at 1273 K for 2 h in an oxygen atmosphere with the heating and cooling rates of 2 K/min.

The density of the sintered pellets was determined with Archimedes' method. For the calculation of relative density, the theoretical density of  $8.46\text{ g/cm}^3$  was used (PDF card no. 032-0522).

The X-ray powder-diffraction (XRD) of the PFN powder after the mechanochemical treatment and crushed sintered pellet were recorded using a PANalytical X'Pert PRO (PANalytical, Almelo, Netherlands) diffractometer with  $Cu-K\alpha_1$  radiation. The XRD patterns were collected over the  $2\theta$  range  $10-70^\circ$ , with a step of  $0.034^\circ$  and 100 s per step.

For the microstructural analysis the samples were fractured for fracture-surface examination, ground and polished using standard metallographic techniques for polish-surface examination and thermally etched at 1023 K for 20 min and fine polishing (by a colloidal silica suspension with  $0.04\ \mu\text{m}$  sized colloidal  $SiO_2$  particles for 1.5 h) for thermally etched-surface examination. The microstructure was studied with a field-emission scanning electron microscope (FE-SEM, JSM-7600F JEOL Ltd., Japan) at 15 kV with a working distance of 15 mm. The grain size and their distribution were determined from the micrographs of the thermally etched samples, where more than 340 grains per sample were measured using the Image Tool Software [20]. The grain size is expressed as the Feret's diameter [21].

For the dielectric measurements, the pellets were cut and thinned to a thickness of about 200  $\mu\text{m}$  and then the Cr/Au electrodes ( $2r = 5 \text{ mm}$ ) were sputtered on samples' surfaces. The dielectric permittivity ( $\epsilon'$ ) at different temperatures was measured with a HP 4284 A Precision LCR impedance meter in the temperature range from 298 K to 473 K.

The EC effect was determined by the indirect method; the EC temperature change ( $\Delta T_{EC}$ ) was calculated from the polarization versus electric field ( $P-E$ ) measured by Aixacct TF analyzer 2000 (Aixacct, Aachen, Germany) at 10 Hz in a temperature range between 298 and 363 K (step 5 K). For the calculation of  $\Delta T_{EC}$  the equation given in ref. [22] was used.

The MC effect was determined by the indirect method; the MC temperature change ( $\Delta T_{MC}$ ) was calculated from the magnetization ( $M$ ) versus temperature measurements at different magnetic fields (1–50 kOe) using a Superconducting Quantum Interference Device magnetometer in a temperature range from 2 to 350 K. The mass of the sample was 30 mg. For the calculation of  $\Delta T_{MC}$  the equation given in ref. [23] was used.

The specific heat capacity ( $C_p$ ), which was needed for the calculation of  $\Delta T_{EC}$  and  $\Delta T_{MC}$  was measured on a 30 mg cube-shaped sample in a temperature range between 2 and 393 K using Physical Property Measurement System.

### 3 Results

The XRD patterns of the PFN powder and crushed pellets are shown in Fig. 1. All the peaks correspond to the perovskite phase (PDF card no. 032-0522) and no

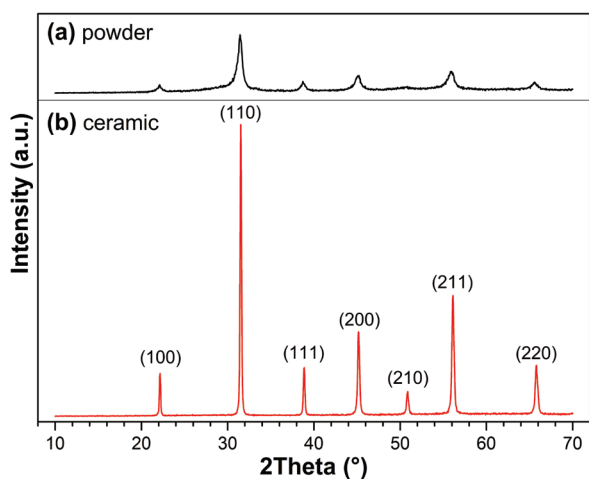


**Figure 1:** XRD patterns of (a) the PFN powder and (b) crushed pellet.

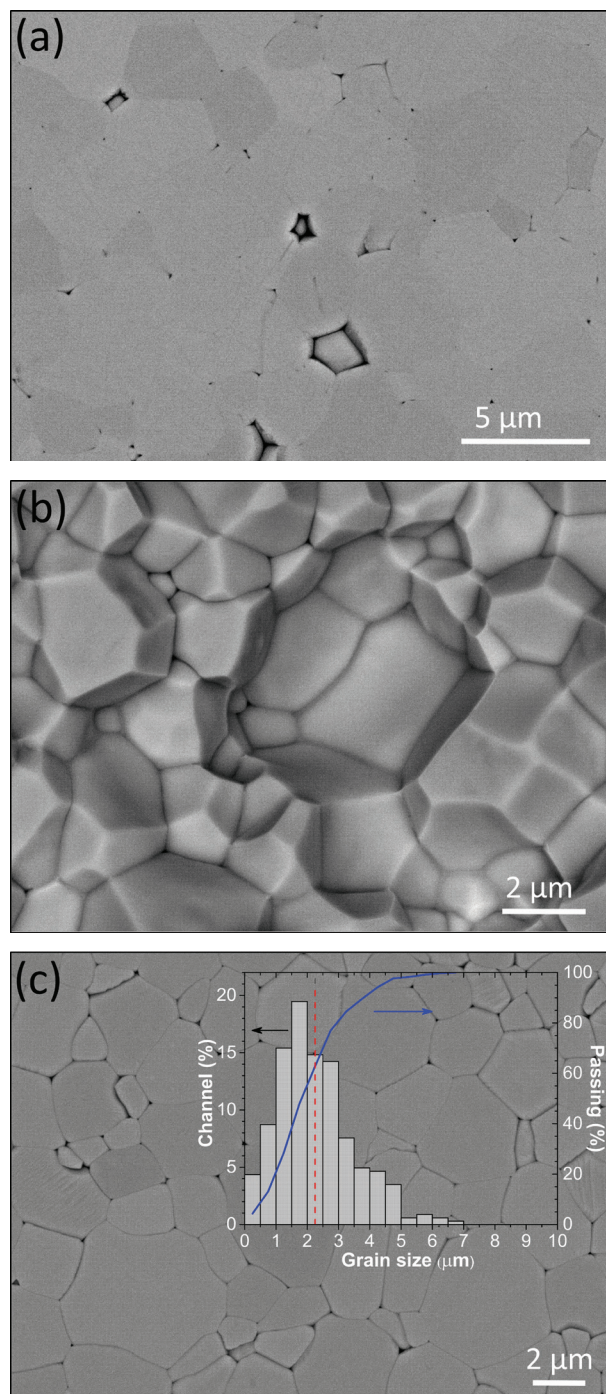


**Figure 2:** (a) Polished, (b) fractured and (c) thermally etched FE-SEM images. Inset: the grain size distribution with the cumulative curve.

secondary phases were observed. Broader diffraction peaks and higher background in the case of powder can be attributed to smaller size of the crystallites and the presence of the amorphous phase, as suggested in [24] for  $\text{Pb}(\text{Mg}_{0.33}\text{Nb}_{0.67})\text{O}_3$ . The density of the ceramic was  $8.1 \text{ g/cm}^3$ , which is equal to 95.7% of the theoretical density.

The FE-SEM micrographs of the polished, fractured and thermally etched surfaces (Figs. 2a-c) of PFN ceramic reveal dense, homogeneous and uniform microstructures with the average grain size of  $(2.3 \pm 1.2) \mu\text{m}$  and unimodal grain size distribution (inset on Fig. 2c). No secondary phases were detected with the FE-SEM analysis in agreement with the XRD analysis.

The temperature dependence of  $\epsilon'$  is shown in Fig. 3. The value at room temperature (298 K) and 1 kHz is 3780. The maximal value of permittivity ( $\epsilon'_{\text{max}}$ ) at 1 kHz is  $\sim 28200$  and it just slightly decreases with increasing frequency ( $\sim 27200$  at 100 kHz). The measured  $\epsilon'_{\text{max}}$  value is higher than previously reported one for solid-state synthesized PFN [25, 26] and comparable with the one for ceramics prepared by mechanochemical synthesis [19].

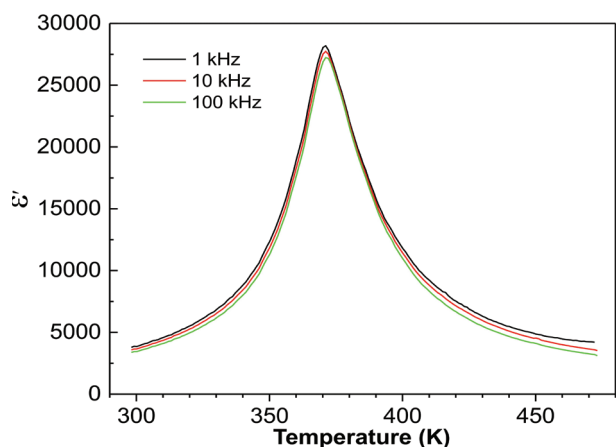


**Figure 3:** Temperature dependence of  $\epsilon'$ .

As shown in Fig. 3 the peak-permittivity temperature ( $T_m$ ) is at 371 K (for all frequencies), which is in agreement with the previously reported ones [26, 27]. According to the literature, this anomaly of  $\epsilon'$  indicates a paraelectric-ferroelectric phase transition [28, 29].

$P$ - $E$  hysteresis loops at different temperatures are shown in Fig. 4a. At room temperature (298 K), typical ferroelectric hysteresis loop is observed. The values of the remanent polarization ( $P_r$ ), maximum polarization ( $P_{\text{max}}$ ) and coercive field ( $E_c$ ) at room temperature are  $\sim 22.5 \mu\text{As/cm}^2$ ,  $\sim 41.6 \mu\text{As/cm}^2$  and  $\sim 4.4 \text{ kV/cm}$ , respectively. The  $P_r$  and  $P_{\text{max}}$  values decreased with the increasing temperature (i.e.,  $P_r \sim 9.1 \mu\text{As/cm}^2$  and  $P_{\text{max}} \sim 35.1 \mu\text{As/cm}^2$  at 363 K).

The temperature dependence of  $\Delta T_{\text{EC}}$  is shown in Fig. 4b. The  $\Delta T_{\text{EC}}$  at room temperature and 80 kV/cm is 0.81 K. The  $\Delta T_{\text{EC}}$  increases with the increasing temperature and increasing applied electric field. The maximum  $\Delta T_{\text{EC}}$  of 1.29 K was obtained at 80 kV/cm and 373 K.

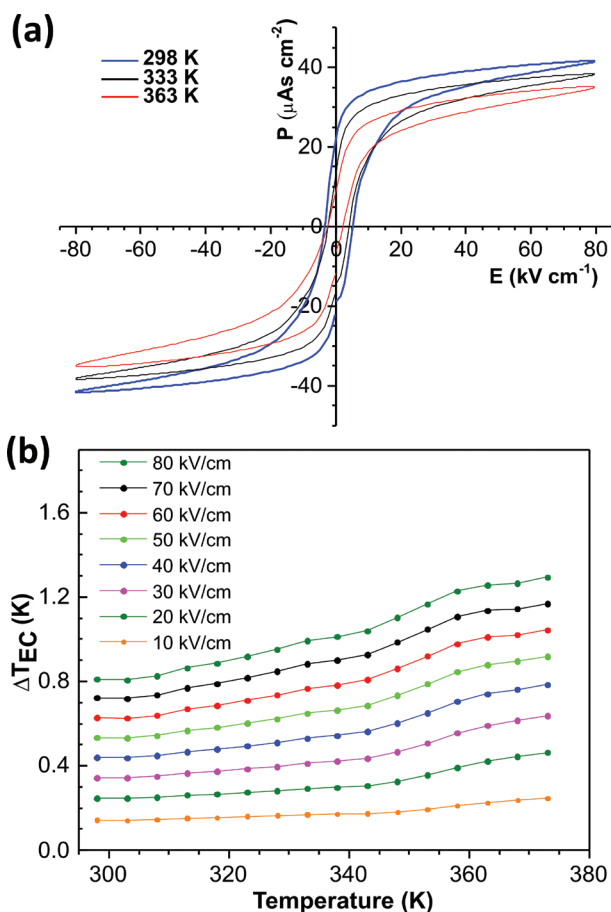


**Figure 4:** (a)  $P$ - $E$  hysteresis loops and (b)  $\Delta T_{\text{EC}}$  versus temperature.

The temperature dependence of  $M$  at different magnetic fields is shown in Fig. 5a. The  $M$  increases with increasing magnetic field and decreasing temperature, therefore the highest value of  $1.37 \text{ Am}^2/\text{kg}$  was observed at 2 K and 50 kOe. Two anomalies are observed in  $M(T, H)$  curves in accordance with the literature [14, 15]. The one at  $\sim 150 \text{ K}$  is attributed to the paramagnetic-antiferromagnetic phase transition, while the second one at  $\sim 10 \text{ K}$  to antiferromagnetic-antiferromagnetic phase transition.

The temperature dependence of  $\Delta T_{\text{MC}}$  is shown in Fig. 5b. The  $\Delta T_{\text{MC}}$  at room temperature and 50 kOe is very low, i.e.,  $\sim 2 \text{ mK}$ . The  $\Delta T_{\text{MC}}$  increases with the decreasing temperature (in proportion to magnetization) and increasing applied magnetic field, therefore the maximum  $\Delta T_{\text{MC}}$  of 0.16 K was obtained at 50 kOe and 2 K.

#### 4 Summary and conclusions

In this work, we were able to prepare single-phase PFN ceramics showing both EC and MC properties. The ce-

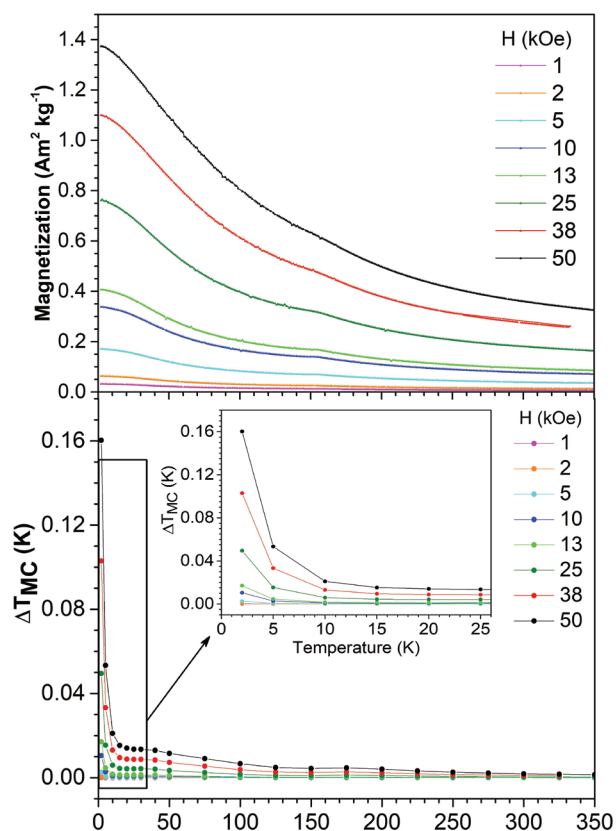


**Figure 5:** (a)  $M$  and (b)  $\Delta T_{MC}$  versus temperature.

ramic pellets were prepared by mechanochemical synthesis of the constituent oxides and thermal treatment at 1237 K. Microstructure analysis revealed dense, homogeneous and uniform microstructures with the average grain size of  $\sim 2.3 \mu\text{m}$ . At room temperature and 1 kHz the value of  $\epsilon'$  was 3780.

The highest value of magnetization (i.e.,  $1.37 \text{ Am}^2/\text{kg}$ ) was measured at low temperature of 2 K. At this temperature also the maximum  $\Delta T_{MC} \sim 0.16 \text{ K}$  was determined. On the other hand, the  $\Delta T_{EC}$  reaches the value as high as 1.29 K at 373 K. But even at room temperature the  $\Delta T_{EC}$  was relatively high, i.e., 0.81 K. Further work is needed in order to confirm EC properties by direct EC temperature measurements, for example by high-resolution calorimetry.

## 5 Acknowledgments

The authors would like to thank the Slovenian Research Agency (research core funding no. P2-0105 and project PR-07594) and joint research project between Polish and Slovenian Academy of Sciences "Multicaloric relaxor materials for new cooling technologies".

## 6 References

1. M. Ozbolt, A. Kitanovski, J. Tusek, A. Poredos, "Electrocaloric vs. magnetocaloric energy conversion," *Int. J. Refrig.* 37, pp. 16–27, 2014.
2. T. Correia, Q. Zhang, Eds., *Electrocaloric materials: New Generation of Coolers*, 1st ed. Berlin, Heidelberg, Germany: Springer-Verlag Berlin Heidelberg, 2014.
3. X. Moya, S. Kar-Narayan, N. D. Mathur, "Caloric materials near ferroic phase transition," *Nat. Mater.* 13, pp. 439–450, 2014.
4. H. Ursic, V. Bobnar, B. Malic, C. Filipic, M. Vrabelj, S. Drnovsek, Y. Jo, M. Wencka, Z. Kutnjak, "A multicaloric material as a link between electrocaloric and magnetocaloric refrigeration," *Sci. Rep.* 6, pp. 26629 1–5, 2016.
5. M. M. Vopson, "The multicaloric effect in multiferroic materials," *Solid State Commun.* 152, pp. 2067–2070, 2012.
6. A. Kumar, K. L. Yadav, "Study on multicaloric effect of CuO induced multiferroic," *J. Appl. Phys.* 116, pp. 083907 1–3, 2014.
7. A. Planes, T. Castan, A. Saxena, "Thermodynamics of multicaloric effects in multiferroics," *Philos. Mag.* 94, pp. 1893–1908, 2014.
8. A. S. Starkov, I. A. Starkov, "Multicaloric Effect in a Solid: New Aspects," *J. Exp. Theor. Phys.* 119, pp. 258–263, 2014.
9. J. K. Murthy, A. Venimadhav, "Multicaloric effect in multiferroic  $\text{Y}_2\text{CoMnO}_6$ ," *J. Phys. D: Appl. Phys.* 47, pp. 445002 1–6, 2014.
10. V. V. Bhat, K.V. Ramanujachary, S. E. Lofland, A. M. Umarji, "Tuning the multiferroic properties of  $\text{Pb}(\text{Fe}_{1/2}\text{Nb}_{1/2})\text{O}_3$  by cationic substitution," *J. Magn. Magn. Mater.* 280, pp. 221–226, 2004.
11. X. Moya, S. Kar-Narayan, N. D. Mathur, "Caloric materials near ferroic phase transitions," *Nat. Mater.* 13, pp. 439–450, 2014.
12. B. Rozic, M. Kosec, H. Ursic, J. Holc, B. Malic, Q. M. Zhang, R. Blinc, R. Pirc and Z. Kutnjak, "Influence of the critical point on the electrocaloric response of relaxor ferroelectrics," *J. Appl. Phys.* 110, pp. 064118 1–5, 2011.
13. R. Havlicek, J. PoltieroVa Vejpravova, D. Bouchenek, "Structure and magnetic properties of perovskite-like multiferroic  $\text{PbFe}_{0.5}\text{Nb}_{0.5}\text{O}_3$ ," *J. Phys. Conf. Ser.* 200, pp. 012058 1–4, 2009.
14. S. Matteppanavar, B. Angadi, S. Rayaprol, "Low temperature magnetic studies on  $\text{PbFe}_{0.5}\text{Nb}_{0.5}\text{O}_3$  multiferroic," *Physica B: Condensed Matter* 448, pp. 229–232, 2014.
15. T. Rojac, A. Bencan, M. Kosec, "Mechanism and Role of Mechanochemical Activation in the Synthesis of  $(\text{K,Na,Li})(\text{Nb,Ta})\text{O}_3$  Ceramics," *J. Am. Ceram. Soc.*, 93, pp. 1619–1625, 2010.

16. H. Ursic, A. Bencan, G. Drazic, G. Esteves, J. L. Jones, T.-M. Usher, T. Rojac, S. Drnovsek, M. DeLuca, J. Jouin, V. Bobnar, G. Trefalt, J. Holc, B. Malic, "Unusual structural-disorder stability of mechanochemically derived-Pb(Sc<sub>0.5</sub>Nb<sub>0.5</sub>)O<sub>3</sub>," *J. Mater. Chem. C*, 3, pp. 10309–10315, 2015.
17. X. Gao, J. Xue, J. Wang, "Sequential Combination of Constituent Oxides in the Synthesis of Pb(Fe<sub>1/2</sub>Nb<sub>1/2</sub>)O<sub>3</sub> by Mechanical Activation," *J. Am. Ceram. Soc.* 85, pp. 565–572, 2002.
18. A. A. Gusev, I. P. Raevski, E. G. Avvakumov, V. P. Isupov, S. I. Raevskaya, H. Chen, V. V. Titov, C.-C. Chou, S. P. Kubrin, S. V. Titov, M. A. Malitskaya, "Dielectric Properties of Undoped and Li-doped Pb(Fe<sub>1/2</sub>Nb<sub>1/2</sub>)O<sub>3</sub> Ceramics Sintered from Mechanochemically Synthesized Powders," *Ferroelectrics* 475, pp. 61–67, 2015.
19. R. Mackeviciute, V. Goian, S. Greicius, R. Grigalaitis, D. Nuzhnyy, J. Holc, J. Banyš, S. Kamba, "Lattice dynamics and broad-band dielectric properties of multiferroic Pb(Fe<sub>1/2</sub>Nb<sub>1/2</sub>)O<sub>3</sub> ceramics," *J. Appl. Phys.* 117, pp. 084101 1–6, 2015.
20. D. Wilcox, B. Dove, B. McDavid, D. Greer, "UTHSCSA Image Tool for Windows version 3.0." University of Texas Health Science Center, San Antonio, 2002.
21. W. H. Walton, "Feret's statistical diameter as a measure of particle size," *Nature*, 162, pp. 329–330, 1948.
22. Z. Kutnjak, B. Rozic, R. Pirc, *Electrocaloric effect: theory, measurements, and applications*, Wiley Encyclopedia of Electrical and Electronics Engineering, John Wiley & Sons, Inc., New Jersey, 2015.
23. A. Kitanovski, J. Tusek, U. Tomc, U. Plaznik, M. Ozbolt, A. Poredos, *Magnetocaloric energy conversion*, ISSN 1865-3529, Springer International Publishing Switzerland, Switzerland, 2015.
24. D. Kuscer, J. Holc, M. Kosec, "Mechano-Synthesis of Lead-Magnesium-Niobate Ceramics," *J. Am. Ceram. Soc.* 89, pp. 3081–3088, 2006.
25. R. Font, O. Raymond-Herrera, L. Mestres, J. Portelles, J. Fuentes, J. M. Siqueiros, "Improvement of the dielectric and ferroelectric properties of multiferroic Pb(Fe<sub>1/2</sub>Nb<sub>1/2</sub>)O<sub>3</sub> ceramics processed in oxygen atmosphere," *J. Mater. Sci.* 51, pp. 6319–6330, 2016.
26. C. C. Chiu, S. B. Desu, "Microstructure and properties of lead ferroniobate ceramics (Pb(Fe<sub>0.5</sub>Nb<sub>0.5</sub>)O<sub>3</sub>)," *Mater. Sci. Eng.*, B21, pp. 26–35, 1993.
27. R. Sun, W. Tan, B. Fang, "Perovskite phase formation and electrical properties of Pb(Fe<sub>1/2</sub>Nb<sub>1/2</sub>)O<sub>3</sub> ferroelectric ceramicse," *Phys. Status Solidi A*, 206, pp. 326–331, 2009.
28. M. Yokosuka, "Electrical and Electromechanical Properties of Hot-Pressed Pb(Fe<sub>1/2</sub>Nb<sub>1/2</sub>)O<sub>3</sub> Ferroelectric Ceramics," *Jpn. J. Appl. Phys.* 32, pp. 1142–1146, 1993.
29. X. S. Gao, X. Y. Chen, J. Yin, J. Wu, Z. G. Liu, "Ferroelectric and dielectric properties of ferroelectromagnet Pb(Fe<sub>1/2</sub>Nb<sub>1/2</sub>)O<sub>3</sub> ceramics and thin films," *J. Mater. Sci.* 35, pp. 5421–425, 2000.

Arrived: 31. 08. 2017

Accepted: 07. 11. 2017

# *Influence of granulate and pressure on green compacts and the current-voltage characteristics of sintered ZnO-based varistor ceramics*

*Slavko Bernik<sup>1</sup>, Matejka Podlogar<sup>1</sup>, Saša Rustja<sup>2</sup>, Mirjam Cergolj<sup>2</sup>*

<sup>1</sup>*Jožef Stefan Institute, Ljubljana, Slovenia*

<sup>2</sup>*VARSIS d.o.o., Ljubljana, Slovenia*

**Abstract:** Granulates G1, G2 and G3, having the same varistor composition but different morphologies in terms of shape, size and size distribution, were characterized for their compactness and flow characteristics. They were also examined during the preparation of disc-shaped green pieces with a diameter of 20 mm by uniaxial pressing at pressures from 3.2MPa to 300MPa. The density and strength of the green samples showed similar pressure dependencies for all the granulates and for the same pressure the green densities were similar. The density of the varistor ceramics sintered at 1200 °C for 2 hours showed little dependence on the compression pressure and the used granulate due to sintering in the presence of a Bi<sub>2</sub>O<sub>3</sub>-rich liquid phase; they already had 93% of theoretical density when pressed at only 10MPa, while for higher pressures the density increased to 96%. The pressure applied during uniaxial pressing also had a small influence on the current-voltage (I-U) characteristics of the varistor ceramics. The varistor ceramics from granulate G1 with the preferred morphology of the granules showed a higher threshold voltage (U<sub>T</sub>) and better I-U nonlinearity (higher coefficient of nonlinearity a) than the ceramics produced from granulates G2 and G3.

**Keywords:** ZnO; varistor ceramics; granulate morphology; compression pressure; strength; electrical properties

## *Vpliv granulata in pritiska na zelene oblikovance in tokovno-napetostne karakteristike sintrane varistorske keramike na osnovi ZnO*

**Izveček:** Analizirali smo kompaktnost in tečljivost granulotov G1, G2 in G3, ki imajo enako varistorsko sestavo in različno morfologijo granul glede oblike, velikosti in porazdelitve velikosti. Preverili smo vpliv granulata na pripravo zelenih kosov v obliki diska s premerom 20 mm pri enosnem stiskanju s pritiski od le 3,2MPa do 300MPa. Pri vseh granulatih se je pokazala podobna odvisnost gostote in trdnosti zelenih oblikovancev od pritiska stiskanja in pri enakem pritisku so imeli podobno gostoto. Gostote varistorske keramike, sintrane pri 1200 °C 2 uri, so pokazale majhno odvisnost od pritiska stiskanja in granulata, kar je posledica sintranja v prisotnosti tekoče faze Bi<sub>2</sub>O<sub>3</sub>; keramika je imela 93% teoretično gostoto že pri stiskanju oblikovancev s pritiskom 10MPa, pri višjih pritiskih stiskanja pa je gostota narasla na 96%. Pritisk enosnega stiskanja ima dokaj majhen vpliv tudi na tokovno-napetostne (I-U) lastnosti varistorske keramike. Varistorska keramika iz granulata G1 z zeleno morfologijo granul je imela višjo prebojno napetost (U<sub>T</sub>) in boljše nelinearnost I-U (višji koeficient nelinearnosti a) kot keramika iz granulotov G2 in G3.

**Ključne besede:** ZnO; varistorska keramika; morfologija granulata; pritisk stiskanja; trdnost; električne lastnosti

\* Corresponding Author's e-mail: [slavko.bernik@ijs.si](mailto:slavko.bernik@ijs.si)

### *1 Introduction*

An exceptional current-voltage (I-U) nonlinearity and a high energy-absorption capability are the reasons why ZnO-based varistors are widely used in the protection of electrical devices, electronic circuits and power sys-

tems against impulse voltage transients over a broad range from a few volts up to several 100 kV. The unique characteristics of ZnO-based varistor ceramics are closely related to their microstructure and arise from the combined effects of the I-U nonlinearity of the

grain boundaries and the high conductivity of the ZnO grains. The nonlinearity results from the electrostatic barriers, which ideally have a breakdown voltage of about 3.2V and are induced by the presence of a  $\text{Bi}_2\text{O}_3$  layer at the grain boundaries. The high conductivity of the grains is obtained by doping the ZnO with oxides of Co, Mn and Ni. The size of the ZnO grains determines the number of grain boundaries at a certain thickness of the ceramic and hence its breakdown voltage, which is the sum of the breakdown voltages of all the non-linear grain boundaries.[1,2] Control of the grain size is therefore important when tailoring the breakdown voltage of the varistor ceramics; hence, either  $\text{Sb}_2\text{O}_3$  or  $\text{TiO}_2$  are usually added to prepare fine-grained, high-voltage or coarse-grained, low-voltage ceramics, respectively.[3] Accordingly, the starting composition of the varistor powder mixture is rather complex, as typically up to about 10% by weight of Bi, Sb, Co, Mn, Ni and Cr oxide is added to the ZnO powder. In the process of sintering at a temperature of about 1200 °C, a complex microstructure is developed, typically composed of the ZnO phase and the secondary phases, the  $\text{Bi}_2\text{O}_3$ -rich phase, the  $\text{Zn}_7\text{Sb}_2\text{O}_{12}$ -type spinel phase and the  $\text{Bi}_3\text{Zn}_2\text{Sb}_3\text{O}_{14}$ -type pyrochlore phase, which has to support the I-U characteristics as required by a particular application. However, sintering is only the final step in processing the varistor ceramics and in such a complex system regarding its chemical composition and the electrical properties, the entire previous history of preparation, especially the proper homogenization of the starting powder mixture for chemical (i.e., compositional) homogeneity and compaction (i.e., pressing) of green molds, also has a strong influence on the final physical properties, much more than with the simpler systems. [4,5]

In the processing of varistors, pieces of varistor ceramic with various dimensions are usually prepared using a standard powder metallurgy procedure with uniaxial pressing of the granulate. Under laboratory conditions, smaller pieces of ceramic can be shaped by pressing the powder or a mixture of powders without or, if necessary, with adding a binder to improve the compressibility and to prevent the formation of cracks or, in the extreme, layering due to internal stresses. The process of shaping must ensure the required repeatability in the production of green bodies without defects, which is requirement in order to obtain ceramics without defects also after sintering. Even with slightly larger samples and in large-scale production this cannot be ensured without the use of granulate, the characteristics of which become the determining factor. The use of a granulate with the appropriate mechanical properties is therefore necessary for the optimization of the pressing process. Spray-drying of the suspension (i.e., the slurry) is typically used in the processing of granu-

late; its characteristics (shape, size, size distribution, density, packing, mechanical strength) are strongly affected by the characteristics of the suspension, which also has to ensure the compositional homogeneity. The granulate must provide excellent compressibility, which means achieving the maximum green density using the lowest possible pressure and an adequate uniformity required for the production of green molds without defects. In order to provide unique compression properties, it is desirable that the granules are round and have a smooth surface. In order to understand what kind of granulate and what kind of granulate properties are required, the processes and mechanisms of granulate deformation during compression need to be known.[6-17]

The pressing of granules usually involves plastic and/or viscoelastic deformations. In the plastic material, the boundary of elasticity, when the material returns to its original condition after load removal, is rapidly reached; with a further load there are irreversible changes. The viscoelasticity is reflected in the viscous and elastic properties. The viscous material resists the load and the strain in material is linearly increasing with the load time. The elastic material, however, deforms under load, but when the load is removed, it can return to its original condition. In the case of granules that exhibit plastic deformation and have different mechanical strengths, some are crushed under the pressure, while those with greater mechanical strength remain whole and cause the formation of a heterogeneous structure with defects. On the other hand, perfectly viscous granules would form perfectly close packing without an applied pressure. This implies that the viscoelastic behavior plays an important role in the compaction process of the granulate. In the process of pressing granulate, first, at low levels of compression pressure, rearrangement of the granules occurs, so that the gaps between them are filled. A further increase in the pressure level tends to increase the remaining tension due to fracture or deformation of the granules. From the viscoelastic deformation of granules, the process of stress release results, which depends on the characteristics of the granules. Thus, the binder-free granules have a lower viscoelastic deformation than those having a binder, which indicates that the compressibility is highly dependent on the binder. With a further increase in the compression pressure, the relaxation tension of the granules increases, thereby increasing the packing density.[6-17]

The influence of the morphology of the granules on the compression quality is reflected in the bending strength of the pieces of ceramic. A higher bending strength comes from ceramics with higher density. A granulate of full granules with a spherical morphology, which allows the preparation of pieces with a higher green density, can contribute to the higher bending strength of ceramics. However, the results showed that a higher density of granules

tends to reduce their compressibility. In the case of green bodies with a density virtually identical to the density of the granules, apparently there was no deformation of the granules in the process of compression; such pieces are non-homogeneous and contain defects that greatly impair the strength of sintered ceramics. The lower-density granules must break down in the compression process to form a homogeneous and compact body. The most appropriate is therefore granulate from spherical and full granules, which exhibit the highest relaxation stress as a result of the viscoelastic deformation; it is a granulate having a lower density of full granules, so that the difference in density between the granules and the green body is a maximum.[6-17]

In this work granulates with different morphologies and same varistor composition were characterized for bulk and tapped density. Their flow characteristics were also determined from the compressibility index and the Hausner ratio. Furthermore, their characteristics when uniaxially pressed were analyzed for pressures ranging from 3.2 MPa to 300 MPa by determining the density and strength of their green compacts. Finally, the influence of the granulate and the compaction pressure on the density and I-U characteristics of ceramics sintered at 1200 °C for 2 hours was studied.

## 2 Experimental

In the study the varistor granulates G1, G2 and G3 with different morphological characteristics were examined and used for the preparation of ZnO-based varistor ceramics. The granulates were prepared using the same spray-drying conditions from stable water slurries having the same composition and amount of varistor powder mixture (i.e., ZnO powder doped with oxides of Bi, Sb, Co, Mn, Ni and Cr) but a different amount of added binder. The bulk density ( $r_0$ ) of the granulates was obtained by adding a known mass ( $m$ ) of granulate to a graduated cylinder to determine the unsettled apparent volume (bulk volume,  $V_0$ ). By mechanically tapping a graduated cylinder containing the sample until little further volume change is observed to obtain the final tapped volume ( $V_f$ ) the tapped density ( $r_f$ ) was obtained. The flow characteristics of the granulates were estimated from the compressibility index (i.e., the Carr index) and the Hausner ratio. The compressibility index was determined using the expression  $Ci = 100(V_0 - V_f)/V_0$  (in %) and the Hausner ratio as  $H_r = V_0/V_f$ . From the studied granulates disc-shaped green compacts having a mass of 3g and a diameter of 20 mm were uniaxially pressed in a stainless-steel die at different pressures of 3.2 MPa, 10 MPa, 50 MPa, 100 MPa, 150 MPa, 200 MPa and 300 MPa. Their green density and strength were determined with respect to the compacting pressure to assess

the influence of the granulate's characteristics. The biaxial flexural strengths of the green samples were measured with a piston-on-three-balls set up, according to the ISO 6872 standard, on a universal testing machine (Quasar 50; Galdabini, Varese, Italy) at a loading rate of 1 mm/min. Microstructures of the fractured surfaces of green pieces shaped at different pressures from granulate G1 after a strength analysis were examined on a scanning electron microscope (SEM, JSM-5800, JEOL, Japan). Green compacts from all the studied granulates and pressed with different pressures were sintered in air at a temperature of 1200 °C for 2 hours. Their sintered densities (as well as their green densities) were measured using a density-measurements system Densitac (Metar sa, Matran, Switzerland). For the DC current-voltage (I-U) characterization, silver electrodes were painted on both parallel surfaces of the discs and fired at 600 °C. The nominal varistor voltages ( $U_N$ ) at 1mA/cm<sup>2</sup> and 10mA/cm<sup>2</sup> were measured using a Keithley 2410 Digital SourceMeter, and the threshold voltage  $U_T$  (V/mm) and the non-linear coefficient  $\alpha$  were determined. The leakage current ( $I_L$ ) was measured at 0.75 $U_N$  (1mA/cm<sup>2</sup>).

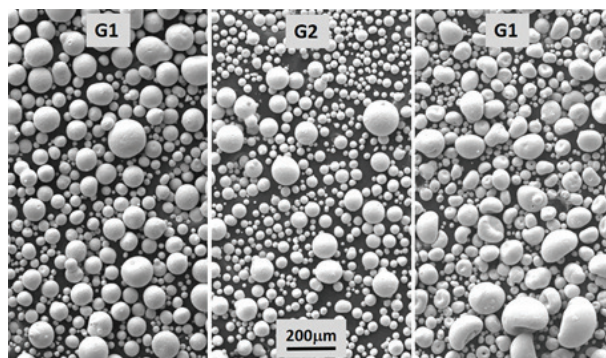


**Figure 1:** SEM images of varistor granulates G1, G2 and G3 showing differences in their morphology.

## 3 Results and discussion

The varistor granulates examined in this work and used for the preparation of the ZnO-based varistor ceramics are shown in Fig. 1. The differences in their morphologies are clearly evident. The granulate G1 has nice spherical granules with quite a uniform size distribution in the range from the smallest of about 10 µm to the largest of about 200 µm. In the granulate G2 the sizes of the smallest and the largest granules are similar to G1; however, the share of smaller granules with sizes in the range from 10 µm to about 50 µm is evidently dominating. The granulate G3 has granules with similar sizes and size distribution as G1; however, the granules have imperfect shapes, often with a crater. While the smaller

granules are full, the larger granules can be either hollow or full in all three granulates, as can be seen in Fig. 2.

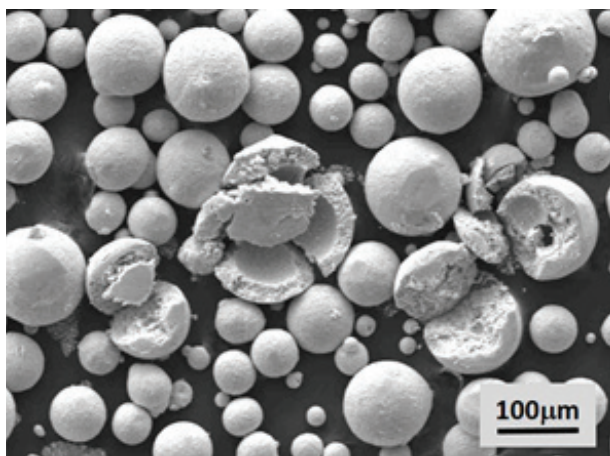


**Figure 2:** SEM image showing that granules, especially larger ones could be either full or hollow.

Table 1 lists the bulk ( $r_o$ ) and tapped ( $r_f$ ) densities of the granulates as well as their flow characteristics estimated from the compressibility index ( $C_i$ ) index and the Hausner ratio ( $H_R$ ) in accordance to the scale given in Table 2. [18] The granulate G1 with a perfect spherical morphology and uniform size distribution of the granules has the highest bulk and tapped densities and an excellent flow characteristic. The granulate G2, which also has perfectly spherical granules, but non-uniform size distribution (i.e., the proportion of small granules predominates), has lower bulk and tapped densities than G1. Nevertheless, according to  $C_i$  and  $H_R$  its flow characteristic is still excellent. However, the granulate G3 with a deformed shape of the granules but a uniform size distribution has similar bulk and higher tapped density than G2, and in regard to its higher  $C_i$  and  $H_R$  values, one level poorer flow properties, classified as good.

**Table 1:** Bulk ( $r_o$ ) and tapped ( $r_f$ ) density of granulates, and their compressibility index ( $C_i$ ) and Hausner ratio ( $H_R$ ) for an estimation of the flow characteristics with respect to the scale given in Table 2

Granulate	$V_o$ (ml)	$V_f$ (ml)	$\rho_o$ (g/ml)	$\rho_f$ (g/ml)	$C_i$ (%)	$H_R$	Flow character
G1	23.25	21.25	1.10	1.20	8.6	1.09	excellent
G2	25.00	23.00	1.02	1.11	8.0	1.09	excellent
G3	25.05	22.00	1.02	1.16	12.2	1.14	good

Regardless of their morphological differences and the differences in their compactness and flow characteristics, all the granulates enable the uniaxial pressing of disc-shaped green compacts with a diameter of 20 mm across a broad range of pressures from the lowest of only

3.2 MPa to the highest of 300 MPa without any difficulties; even after pressing with the lowest pressures the green compacts from all the granulates were compact enough for subsequent handling without any problem and at the highest pressure no lamination of the discs was observed. The density of the green compacts from the granulate G1 with respect to the pressure of the uniaxial pressing is given in Fig. 3; the density rapidly increased with pressure up to 50 MPa to about 3 g/cm<sup>3</sup>, while with further increasing of pressure the density increased steadily to the value of about 3.6 to 3.7 g/cm<sup>3</sup> at 300 MPa. Practically same green densities for the given pressure and the same dependence of the green density on the pressure were obtained also for the granulates G2 and G3.

**Table 2:** Flow properties of solids with respect to their Carr index (i.e., compressibility index) and Hausner ratio.[18]

Carr's index (%)	Flow character	Hausner ratio
1-10	Excellent	1.00-1.11
1-15	Good	1.12-1.18
16-20	Fair	1.19-1.25
21-25	Passable	1.26-1.34
26-31	Poor	1.35-1.45
32-37	Very poor	1.46-1.59
>38	Very, very poor	>1.60

The strengths of the green pieces prepared at different pressures of uniaxial pressing are given in Fig. 4. All the granulates show a similar dependence of the strength on the pressure. However, while the samples from granulates G2 and G3 have similar strengths at all pressures, it is higher for the samples from granulate G1 and the difference increases with increasing pressure. After pressing with 300 MPa the samples G1 have a strength of about 17 MPa and the samples G2 and G3, of about 13 MPa.

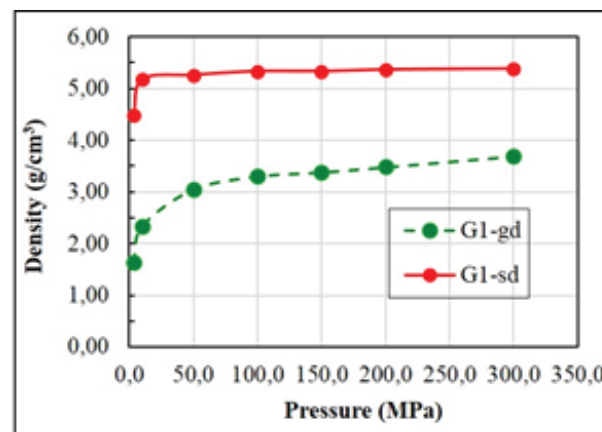


**Figure 3:** Green-density (G1-gd) and density after sintering at 1200 °C (G1-sd) of samples from the granulate G1 with respect to the pressure of uniaxial pressing.

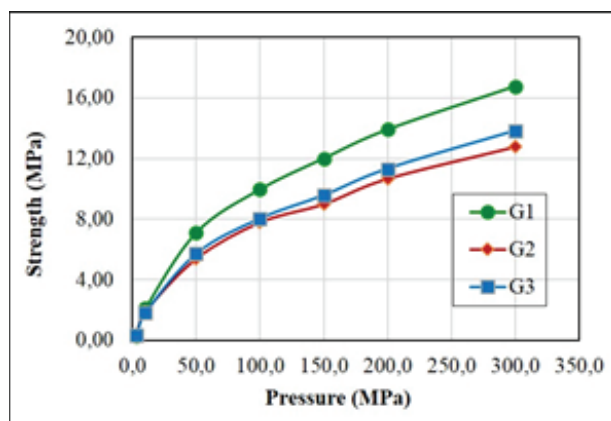


**Figure 4:** Strength of the green compacts from granulates G1, G2 and G3 with respect to the pressure of uniaxial pressing.

Microstructures of a fractured surface of the green samples from the granulate G1, uniaxially pressed at different pressures are presented in Fig. 5. After a pressure of 3.2 MPa the granules remain whole, while being slightly indented into each other so that porosity among them is still evident, which still ensures sufficient compactness for the green samples to be handled without difficulties. At a pressure of 10 MPa the shape of the individual granules is still clearly evident, the degree of indentation among the granules is already much larger so that the remaining porosity among them is already much lower and some granules are already partially collapsed. However, already after a pressure of 50 MPa the microstructure of the fractured surface is perfectly homogeneous as all the granules are fully collapsed so that their shape was not distinct anymore. With a further increase of the pressure the microstructure of fractured surface remains the same.

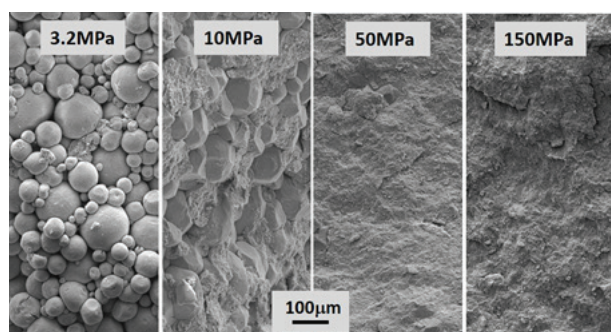


**Figure 5:** Microstructures of fractured surface of green samples pressed from granulate G1 at different pressures.

The densities of the varistor ceramics from the granulate G1, uniaxially pressed at different pressures and sintered at 1200 °C for 2 hours, are graphically presented in Fig. 3. Interestingly, already the samples pressed with only 3.2 MPa had a sintered density of about 4.5 g/cm<sup>3</sup> (i.e.,

about 80% of theoretical density). However, for a pressure of just 10 MPa the density of the sintered ceramics increased to about 5.2 g/cm<sup>3</sup> (93 % t.d.) and with further increasing of the pressure this only slightly increased to about 5.4 g/cm<sup>3</sup> (96 % t.d.). The sintered ceramics from the granulates G2 and G3 had a similar density at a certain pressure and a similar dependence of the density on the compression pressures as the ceramics from the granulate G1. Such results, which showed very little influence of the granulate morphology and the pressure of uniaxial pressing on the density, could be explained by the sintering of the varistor ceramics, which takes place in the presence of the Bi<sub>2</sub>O<sub>3</sub>-rich liquid phase.

The current-voltage (I-U) characteristics of the varistor ceramics from granulates G1, G2 and G3, uniaxially pressed at different pressures and sintered at 1200 °C for 2 hours are presented in Figs. 6 and 7. Surprisingly, very little influence of the compression pressure on the I-U characteristics was observed. Only in the ceramics pressed with 3.2 MPa were noticeably different values of the threshold voltage ( $U_T$ ) and the coefficient of nonlinearity ( $\alpha$ ) observed, while already for a pressure of 50 MPa and higher they were similar for the ceramics from all three granulates. However, the ceramics from granulate G1 had a higher  $U_T$  (about 125 V/mm) than the ceramics from the granulates G2 and G3 with values around 108 V/mm (Fig. 6). Also, the ceramics from granulate G1 had a much higher  $\alpha$  of about 34 in comparison to values of about 20 for the ceramics from the granulates G2 and G3 (Fig. 7). Actually, in the ceramics from granulate G3 the value of  $\alpha$  increases with a higher compression pressure from 19 at 10 MPa to 23 at 300 MPa. Interestingly,  $\alpha$  in the ceramics from granulates G2 and G3 pressed with only 3.2 MPa is higher (25) than at higher pressures. In varistor ceramics from all the studied granulates the leakage current ( $I_L$ ) is similar in the range from 4 to 8  $\mu$ A, regardless of the pressure of the uniaxial pressing.

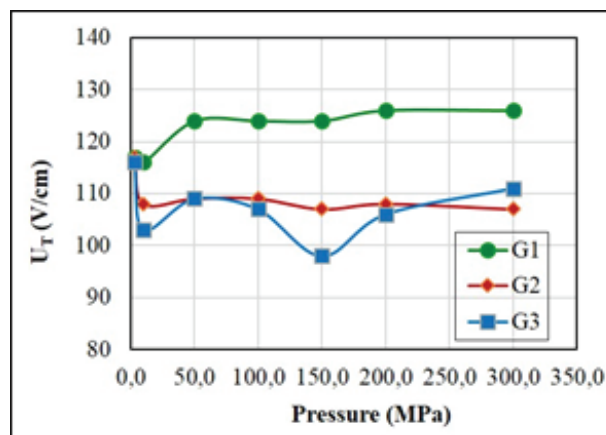


**Figure 6:** Threshold voltage  $U_T$  (V/mm) of the varistor ceramics from granulates G1, G2 and G3, uniaxially pressed at different pressures and sintered at 1200 °C for 2 hours.

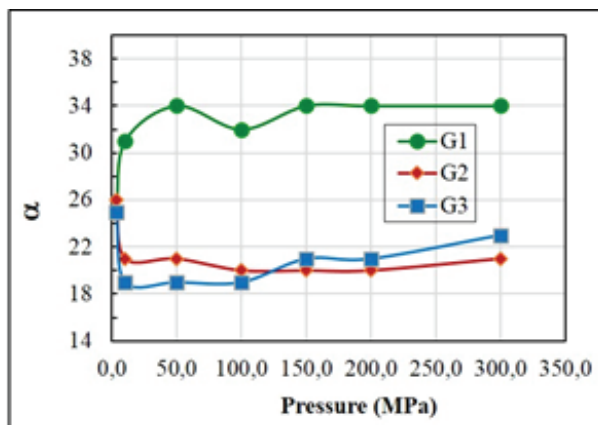


**Figure 7:** Coefficient of nonlinearity  $\alpha$  of the varistor ceramics from granulates G1, G2 and G3, uniaxially pressed at different pressures and sintered at 1200 °C for 2 hours.

## 4 Conclusions

In this work granulates G1, G2 and G3, having the same composition of the varistor powder mixture and different morphologies of the granules, were characterized for their compacting and flow characteristics. Granulate G1 with a uniform size distribution of spherical granules had the highest bulk and tapped densities, and according to the Carr index ( $C_i$ ) and Hausner ratio ( $H_R$ ) they also had excellent flow characteristics. The granulate G2 with the spherical granules but the non-uniform size distribution due to a dominant fraction of smaller granules also had excellent flow characteristics, while the granulate G3 with a uniform size distribution but deformed granules qualified for flow characteristic as good. All the granulates showed good properties in terms of the uniaxial pressing of green bodies for pressures in the range from only 3.2 MPa to 300 MPa; green pieces could be handled without difficulties and no lamination occurred. For all the granulates the density and strength of green samples showed similar dependence to the pressure and for the same pressure the green densities were similar. The samples from G1 with a preferred morphology of the granules had a higher strength. The density of varistor ceramics sintered at 1200 °C for 2 hours showed very little dependence on the compression pressure and the granulate used, and reached 93% of the theoretical density already when pressed with only 10MPa, while for higher pressures the density increased to 96%. This could be explained by the sintering of the varistor ceramics in the presence of the  $\text{Bi}_2\text{O}_3$ -rich liquid phase. Accordingly, also a relatively low influence of compression pressure on the current-voltage (I-U) characteristics of the varistor ceramics was observed. However, the varistor ceram-

ics from the granulate G1 showed a higher threshold voltage ( $U_T$ ) and a better I-U nonlinearity (higher coefficient of nonlinearity  $\alpha$ ) than the ceramics from the granulates G2 and G3. The reasons can be found in their microstructure, which should be thoroughly examined in the future.

## 5 References

1. T. K. Gupta, Application of zinc oxide varistors, *J. Am. Ceram. Soc.*, vol. 73, no. 7, pp. 1817-1840, 1990.
2. D. R. Clarke, Varistor ceramics, *J. Am. Ceram. Soc.*, vol. 82, no. 3, pp. 485-502, 1999.
3. S. Bernik, N. Daneu, A. Rečnik, Inversion boundary induced grain growth in  $\text{TiO}_2$  or  $\text{Sb}_2\text{O}_3$  doped ZnO-based varistor ceramics, *J. Eur. Ceram. Soc.*, vol. 24, pp. 3703-3708, 2004.
4. M. Inada, Formation Mechanism of nonohmic zinc oxide ceramics, *Jpn. J. Appl. Phys.*, vol. 19, no. 3, pp. 409-419, 1980.
5. M. L. Arefin, F. Raether, D. Dolejš, A. Klimera, Phase formation during liquid phase sintering of ZnO ceramics, *Ceram. Int.*, vol. 35, pp. 3313-3320, 2009.
6. J. Tsubaki, H. Yamakawa, T. Mori, H. Mori, Optimisation of granulates and slurries for press forming, *J. Ceram. Soc. Jpn.*, vol. 110, no. 10, pp. 894-898, 2002.
7. M. Naito, Y. Fukuda, N. Yoshikawa, H. Kamiya, J. Tsubaki, Optimisation of suspension characteristics for shaping processes, *J. Eur. Ceram. Soc.*, vol. 17, pp. 251-257, 1997.
8. S. J. Lukasiewicz, Spray-drying ceramics powders, *J. Am. Ceram. Soc.*, vol. 72, no. 4, 617-624, 1989.
9. W. J. Walker Jr., J. S. Reed, S. K. Verma, Influence of slurry parameters on the characteristics of spray-dried granules, *J. Am. Ceram. Soc.*, 82, no. 7, p.p. 1711-1719, 1999.
10. H. Takahashi, N. Shinohara, M. Okumiya, K. Uematsu, T. Junichiro, Y. Iwamoto, H. Kamiya, Influence of slurry flocculation on the character and compaction of spray-dried silicon nitride granules, *J. Am. Ceram. Soc.*, vol. 78, no. 4, p.p. 903-908, 1995.
11. V. Naglieri, D. Gutknecht, V. Garnier, P. Palmero, J. Chevalier, L. Montanaro, Optimised slurries for spray drying: Different approaches to obtain homogeneous and deformable alumina-zirconia granules, *Materials*, vol. 6, p.p. 5382-5397, 2013.
12. G. Bertrand, P. Roy, C. Filiatre, C. Codder, Spray-dried ceramic powders: A quantitative correlation between slurry characteristics and shapes of the granules, *Ceram. Eng. Sci.*, vol. 60, p.p. 95-102, 2005.

13. K. Uematsu, J. Y. Kim, M. Miyashita, N. Uchida, K. Saito, Direct observation of internal structure in spray-dried alumina granules, *J. Am. Ceram. Soc.*, vol. 73, no. 8, p.p. 2555-2557, 1990.
14. M. Naito, K. Nakahira, T. Hotta, A. Ito, T. Yokoyama, H. Kamiya, Microscopic analysis on the consolidation process of granule beds, *Powder Tech.*, vol. 95, p.p. 214-219, 1998.
15. J. L. Amoros, V. Cantavella, J. C. Jarque, C. Feliu, Fracture properties of spray-dried powder compacts: Effect of granule size, *J. Eur. Ceram. Soc.*, vol. 28, p.p. 2823-2834, 2008.
16. M. I. Zainuddin, S. Tanaka, R. Furushima, K. Uematsu, Correlation between slurry properties and structures and properties of granules, *J. Eur. Ceram. Soc.*, vol. 30, p.p. 3291-3296, 2010.
17. M. Uppalapati, D. J. Green, Effect of relative humidity on the viscoelastic and mechanical properties of spray-dried powder compacts, *J. Am. Ceram. Soc.*, vol. 89, no. 4, p.p. 1212-1217, 2006.
18. R. L. Carr, Evaluating flow properties of solids, *Chem. Eng.*, vol. 72, pp. 163-168, 1965.

Arrived: 31. 08. 2017

Accepted: 15. 11. 2017



# Processing and sintering of sodium-potassium niobate-based thick films

Hugo Mercier<sup>1,2,3</sup>, Barbara Malič<sup>1,2</sup>, Hana Uršič<sup>1</sup>, Danjela Kuscer<sup>1</sup>, Franck Levassort<sup>3</sup>

<sup>1</sup>Jožef Stefan Institute, Electronic Ceramics Department, Ljubljana, Slovenia

<sup>2</sup>Jožef Stefan International Postgraduate School, Ljubljana, Slovenia

<sup>3</sup>GREMAN UMR-CNRS 7347, Université de Tours, INSA Centre Val de Loire, Tours, France

**Abstract:** The electrophoretic deposition (EPD) and sintering of  $(K_{0.5}Na_{0.5})_{0.99}Sr_{0.005}NbO_3$  (KNNSr) thick films on platinized alumina substrate is reported. We demonstrate that by a two-step deposition-sintering the KNNSr films thicker than 30  $\mu\text{m}$  without defects can be prepared. The effect of the sintering time on structural, microstructural, dielectric and electromechanical characteristics of the KNNSr thick films is discussed. By increasing the sintering time from 2 to 4 hours, the density and the dielectric permittivity of the thick films increased. The unit cell parameters of the perovskite phase decreased which could be related to the formation of polyniobate and volatilization of alkalis. Processed KNNSr exhibited promising electromechanical and piezoelectric properties, with a thickness coupling factor up to 35 % and piezoelectric coefficient  $d_{33}$  up to 80 pC/N.

**Keywords:** sodium potassium niobate; electrophoretic deposition; thick films, piezoelectric properties; electromechanical properties

## Priprava in sintranje debelih plasti na osnovi natrijevega kalijevega niobata

**Izveček:** Študirali smo sintranje debelih plasti  $(K_{0.5}Na_{0.5})_{0.99}Sr_{0.005}NbO_3$  (KNNSr), ki smo jih na metalizirani korundni podlagi pripravili z metodo elektroforetskega nanosa. Pokazali smo, da z dvostopenjskim nanosom in sintranjem lahko pripravimo plasti KNNSr debelejšje od 30  $\mu\text{m}$  in brez defektov. V prispevku poročamo o vplivu časa sintranja plasti KNNSr na njihovo strukturo, mikrostrukturo ter dielektrične in elektromehanske lastnosti. Gostota in dielektrična konstanta plasti KNNSr se povečata s podaljšanjem časa sintranja od 2 na 4 ure, parametri perovskitne osnovne celice pa se zmanjšajo, kar pripisujemo tvorbi sekundarne faze poliniobata in izhajanju alkalijskih oksidov med sintranjem. Plasti KNNSr imejo obetajoče elektromehanske in piezoelektrične lastnosti: povprečni sklopitveni faktor je 35 %, piezoelektrični koeficient  $d_{33}$  pa do 80 pC/N.

**Ključne besede:** natrijev kalijev niobat; elektroforetski nanos; debele plasti; piezoelektrične lastnosti; elektromehanske lastnosti

\* Corresponding Author's e-mail: hugo.mercier@univ-tours.fr

### 1 Introduction

Piezoelectric energy harvester (PEH) allows the conversion of mechanical energy into electrical energy which can power wireless, self-powered microsystems and macroscale devices [1, 2]. A typical PEH structure is a bimorph cantilever with two layers of piezoelectric material on both sides of a flexible substrate.

Piezoelectric layers of lead-based materials, typically lead zirconate titanate, have been mainly used due to their outstanding piezoelectric properties [3]. However due to lead toxicity and environmental problem there is a need to replace them with environment-benign

material. Among the lead-free piezoelectric materials, potassium sodium niobate  $((K_{0.5}Na_{0.5})NbO_3 - KNN)$  have been extensively studied. The processing of a dense single phase KNN ceramics is challenging, due to the hygroscopic nature of the raw material, the narrow temperature range of sintering, and the volatilization of alkaline species at the processing temperature [4]. Literature reports that addition of 0.5 % Sr, as A-site donor dopant,  $((K_{0.5}Na_{0.5})_{0.99}Sr_{0.005}NbO_3 - KNNSr)$  improves the density and dielectric/piezoelectric properties of the material ( $d_{33} \sim 80$  pC/N,  $k_t \sim 0.4$ , dielectric permittivity  $\sim 500$  and dielectric losses  $\sim 0.03$ ) [4, 5].

Bimorph cantilever PEH have been often prepared by thinning piezoelectric bulk ceramics from a few hundreds to tens of micrometers and consequent gluing of slices [7,8] onto a substrate. This process is complicated and time consuming. Another possibility is to process the thick piezoelectric films directly onto a conductive substrate using thick film technologies. Among them, electrophoretic deposition (EPD) [9] allows the deposition of piezoelectric thick films within a few minutes onto complex-shape substrates. EPD is suitable method for processing a cantilever, since the deposition can be done simultaneously on the top and bottom side of the substrate.

KNN-based thick films have been prepared by EPD using ethanol-, acetone- and water-based suspensions [10–12]. In a previous work, the processing of KNNSr thick films prepared from ethanol-based suspension, and sintered at 1100 °C for 2 hours in air, was reported. The processed thick films were around 25 µm thick and they exhibited a relative density of 75 %, a dielectric constant of 294, dielectric losses of 0.05 at 1 MHz at 20 °C and a  $d_{33}$  of 60 pC/N [12].

The lower density of thick films compared to bulk ceramic can be related to the sintering of the thick film in constrained conditions. The clamping of the thick film on the substrate may result in a tensile stress which hindered the densification of the layers [13, 14]. The stresses relax through growth of defects and or/delamination of the thick film from the substrate [15].

In order to improve the density and functional properties of KNN-based thick films, the effect of sintering conditions were studied. It was shown that density of KNN-based material increases with the sintering time [16], but larger time may lead to the formation of larger amount of secondary phases [17]. Sintering of KNN-based ceramics in oxygen atmosphere showed several advantages compared to sintering in air: increased density [18], limited amount of secondary phases [17], reduced oxygen vacancy concentration and improved electromechanical properties [19, 20].

The aim of this work was to process KNNSr thick films on platinized alumina substrate by EPD with final thickness greater than 30 µm. In this case the use of a two steps deposition-sintering process was developed. Moreover the effect of sintering time, i.e., 2 and 4 hours, on the structure, microstructure, dielectric and electromechanical properties of the thick films was studied.

## 2 Experimental

( $K_{0.5}Na_{0.5}$ )<sub>0.99</sub>Sr<sub>0.005</sub>NbO<sub>3</sub> (KNNSr) powder was prepared by solid-state synthesis as described elsewhere [21]. Bulk KNNSr ceramics was prepared by compacting KNNSr powder with a uniaxial press into cylindrical samples, followed by cold isostatically pressing at 200 MPa and sintering at 1120 °C in air with heating and cooling rates of 5 K/min.

The suspension was prepared by mixing 1 vol % of the KNNSr powder in absolute ethanol (C<sub>2</sub>H<sub>5</sub>OH, anhydrous, Carlo Ebra, Italy) with 50 µmol/g poly(acrylic acid-co-maleic acid) (Mw 3.000, 50 wt % water solution, Sigma Aldrich, Germany) and 100 µmol/g n-butylamine (Alfa Aesar, Germany), as detailed in [12].

The substrate acting as a working electrode was prepared by screen-printing platinum paste (Ferro 1192, USA) onto an alumina substrate (A493, Kyocera, Japan). The paste was deposited on a region of 8 x 8 mm and fired at 1200 °C for 1 hour in air. The counter electrode was a platinum disc (thickness of 0.1 mm and diameter of 8 mm).

EPD were performed in a custom-made setup at a constant current density of 1.56 A/cm<sup>2</sup> provided by a Keithley 2400 source meter. The layers were deposited either in a single step for 120 s (sample denoted KNNSr-R) or in two steps. In two steps deposition, the first step included the deposition of KNNSr for 60 s, and the presintering of as-deposited layers at 1000 °C for 2 h in oxygen with heating and cooling rate of 2K/min. Samples were denoted KNNSr-L. In the second step, second layers were deposited onto KNNSr-L for 60 s and afterward sintered at 1100 °C in oxygen for 2 hours (sample denoted KNNSr-2h) and 4 hours (sample denoted KNNSr-4h).

The X-ray powder-diffraction data (XRD) were collected in the 2θ range from 20° to 60° in steps of 0.034°, by PANalytical diffractometer (X'Pert PRO MPD, The Netherlands). The phases were identified using the software X-Pert High Score and the PDF-2 database [22]. The unit cell parameters were refined using JANA2006 software, by performing a full pattern matching, assuming a *P1m1* space group. A zero-error shift correction was used to obtain the correct initial position, the background was calculated using a Legendre polynomial and the peak profiles were refined using a pseudo-Voigt function.

The polished cross-sections of the sintered films were analyzed using scanning electron microscopes (SEM, JSM-5800 and JSM 7600F, both JEOL, Japan).

Gold electrodes, with a diameter of 1.5 mm and a thickness of ~100 nm, were sputtered (5 Pascal, Italy) on top of the sintered samples. The capacitance and dielectric losses ( $\tan \delta$ ) were measured in the frequency range 10 kHz-1 MHz at room temperature with an impedance spectroscopy analyzer (4192A Hewlett Packard, USA). Samples were poled for 40 min at 120 °C with a DC-electric field of 3 kV/mm. The piezoelectric constants  $d_{33}$  were measured with a Berlincourt piezometer (Take Control PM10, Birmingham, UK).

The complex electrical impedance, around the fundamental thickness mode was measured using a vector analyzer (HP4395) and its impedance test kit. A theoretical model, based on the Krimholtz-Leedom-Matthaei (KLM) equivalent electrical circuit [23], delivers the theoretical complex impedance of the thickness mode as a function of the frequency. By fitting the experimental data with the theoretical model, the thickness mode parameters of the KNNSr sintered and poled thick films are deduced. The modeled structure was composed of 3 layers: the alumina substrate; the Pt bottom electrode and the thick piezoelectric film. The top gold electrode was neglected as it was too thin to have a significant effect. The parameters of the inert layers [24] and the thickness of the piezoelectric films are considered as fixed in the model. The following parameters were deduced: the thickness coupling factor  $k_t$ , the longitudinal wave velocity  $v_l$ , the dielectric constant at constant strain  $\epsilon_{33}^s/\epsilon_0$  and the tangent of the dielectric loss angle  $\delta_e$ .

### 3 Results and discussion

#### 3.1 Processing of KNNSr thick films

Sample KNNSr-R, deposited in a single step, exhibited defects at its surface, resulting in shortcuts, preventing the electrical measurements, see Figure 1.a. The thickness of the as-deposited layer KNNSr-R was around 60  $\mu\text{m}$  and around 40  $\mu\text{m}$  after sintering. This thickness was presumably above the critical thickness thus defects occurred during the drying and/or the sintering of the thick film [25,26]. In order to process defect-free thick films with final thicknesses above 30  $\mu\text{m}$ , a two steps process was used. A first layer was deposited and pre-sintered (KNNSr-L). KNNSr-L had a deposited yield of  $3.5 \pm 0.5 \text{ mg/cm}^2$  and a sintered thickness of  $18 \pm 5 \mu\text{m}$  and did not exhibit large defects after its processing (Figure 1.b).

The second layer was deposited on the top of the first one (60 s) and sintered at selected conditions given for KNNSr-2h and KNNSr-4h. The cumulative deposition time for the two layers was the same as for KNNSr-R,

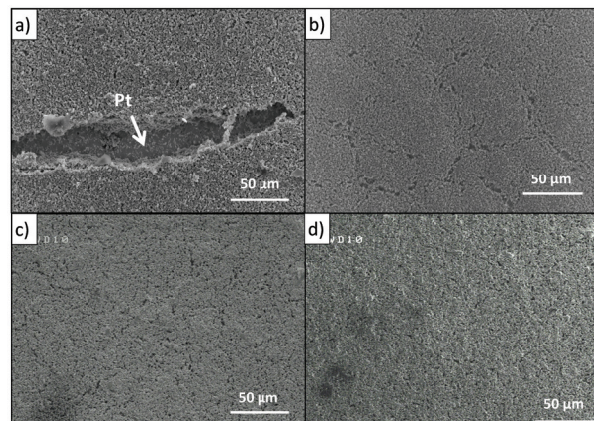


**Figure 1:** SEM image of the surface of sintered KNNSr thick films a) KNNSr-R b) KNNSr-L c) KNNSr-2h and d) KNNSr-4h.

i.e., 120 s. The processed thick films prepared with the described procedure did not exhibit large defects at their surfaces (Figure 1.c and d).

#### 3.2 Sintered KNNSr thick films

The XRD patterns of the thick films sintered for 2 (KNNSr-2h) and 4 hours (KNNSr-4h) are presented in Figure 2. Both samples consisted of a main monoclinic perovskite phase indexed as  $\text{K}_{0.65}\text{Na}_{0.35}\text{NbO}_3$  (PDF: 77-0038), and a polyniobate phase indexed as  $\text{K}_{5.75}\text{Nb}_{10.85}\text{O}_{30}$  (PDF: 38-0297). In addition the diffraction peaks of the top gold electrode and of the platinum bottom electrode were also observed on the diffraction pattern. The formation of the polyniobate phase, which was not identified in the initial powder, may be related to the volatilization and segregation of alkaline species [4].

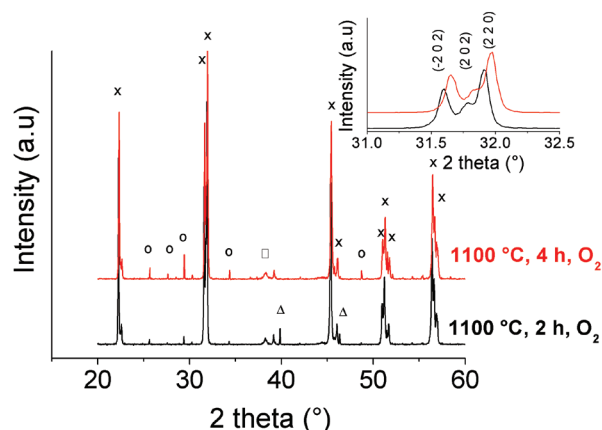


**Figure 2:** XRD patterns of KNNSr thick films sintered at 1100 °C in oxygen for 2 and 4 hours. x:  $\text{K}_{0.65}\text{Na}_{0.35}\text{NbO}_3$  (PDF: 77-0038), o:  $\text{K}_{5.75}\text{Nb}_{10.85}\text{O}_{30}$  (PDF: 38-0297),  $\Delta$ : Platinum (PDF:04-0802),  $\square$ : Gold (PDF: 01-1172).

The calculated cell parameters for the samples KNNSr-2h and KNNSr-4h are presented in Table 1. The calculated unit cell parameters exhibited lower values than the one reported in the literature for bulk ceramics with the same composition [27]. The reduction in the unit cell parameters may be attributed to two phenomena. First phenomenon was the loss of alkali oxides during the sintering. Literature reports that potassium vapor pressure above KNN is greater than sodium one [28,29]. Since potassium ions have a larger radius ( $K^+$ , 0.164 nm) than sodium ions ( $Na^+$ , 0.139 nm) the perovskite with K/Na ratio smaller than 1 resulted in a decrease of the unit cell parameters of the perovskite phase [29,30]. In the case of a thick film this phenomenon is expected to be enhanced due the increased area to volume ratio in comparison to bulk ceramic. The second phenomenon was the formation of a polyniobate phase, clearly observed on the XRD spectra. The polyniobate phase had a potassium-rich composition, thus the perovskite phase could have lower potassium content and this again decreased the unit cell parameters of the perovskite phase. On XRD patterns peaks attributed to the polyniobate phase had higher intensity in the samples KNNSr-4h in comparison to KNNSr-2h which indicated the presence of a larger amount of polyniobate phase and may explain the further reduction in the unit cell parameters of KNNSr-4h.

The polished cross-section SEM images of the sintered thick films KNNSr-2h and KNNSr-4h, are presented in Figure 3.a and b, respectively. The microstructure of the samples consisted of micrometers sized pores randomly distributed in a KNNSr particles matrix, see insets Figure 3. Phase composition by EDXS showed that the matrix is a perovskite with K/Na ratio of about 1. Larger grains (see black arrows on the SEM images) had a K/Na ratio greater than 1 and were presumably polyniobate phase. The relative density, estimated from the SEM images were  $77 \pm 4\%$  and  $87 \pm 4\%$  for KNNSr-2h and KNNSr-4h, respectively. This showed that by increasing the sintering time from 2 to 4 hours, the density of the thick films increased by 10 %. The thickness of KNNSr-2h and KNNSr-4h were 33 and 45  $\mu\text{m}$ , respectively. The discrepancy in the thickness was attributed to the variation in the as-deposited layers thickness, i.e.  $\pm 5\mu\text{m}$ , for each deposited layer.

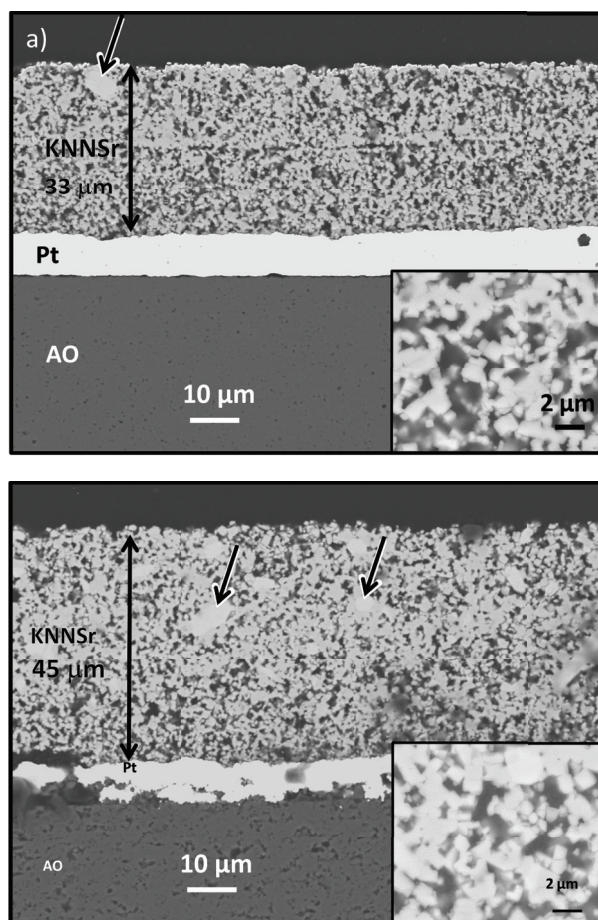


**Figure 3:** Polished cross-section SEM images of KNNSr thick films sintered at 1100 °C in oxygen for a) 2 hours (KNNSr-2h) and b) 4 hours (KNNSr-4h). The insets show KNNSr thick films microstructures at larger magnification; the black arrows show examples of larger grains (polyniobate).

### 3.3 Functional characterizations

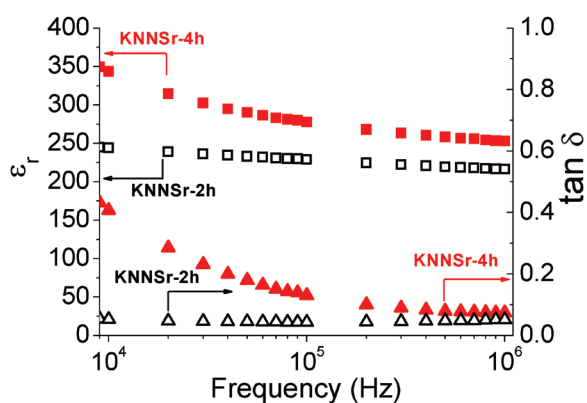
The dielectric measurements of the thick films are presented in Figure 4. The permittivity and losses decreased with increasing frequency. Values of KNNSr-4h permittivity and losses are higher than those of KNNSr-2h in the same measured frequency range. The dielectric permittivity and losses at 100 kHz were 230 and 0.04, respec-

**Table 1:** Refined unit cell parameters of the KNNSr thick films sintered at 1100 °C in oxygen for 2 h (KNNSr-2h) and 4 h (KNNSr-4h) and unit cell parameters reported for the KNNSr ceramics.

Sample	a	b	c	$\beta$	V
	[nm]	[nm]	[nm]	[°]	[nm <sup>3</sup> ]
KNNSr-2h	0.40028(9)	0.39443(6)	0.39961(9)	89.70(2)	0.06309(4)
KNNSr-4h	0.40016(9)	0.39431(6)	0.39946(9)	89.69	0.06303(2)
KNNSr bulk [27]	0.400375	0.394596	0.399938	90.3228	0.06318
Estimated error	$\pm 0.0001$	$\pm 0.0001$	$\pm 0.0001$	$\pm 0.001$	$\pm 0.00002$

**Table 2:** Properties of thick piezoelectric films KNNSr-2h, KNNSr-4h, KNNSr bulk ceramic and KNN-based screen printed thick films.

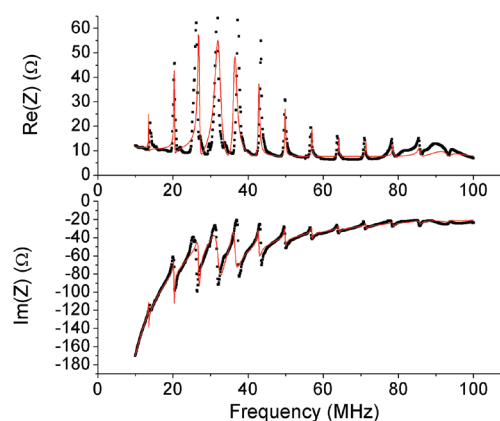
Sample	Thickness	$k_t$	$\epsilon_{335}/\epsilon_0$	$\delta_e$	$d_{33}$
	[ $\mu\text{m}$ ]	[%]		[%]	[pC/N]
KNNSr-2h	33	35	155	3	80
KNNSr-4h	45	32	165	5	80
KNNSr-bulk ceramic 1120 °C, 2 h, air	/	40	300	5	90
KNN-based screen printed thick films [32]	43	30	140	/	/

**Figure 4:** Dielectric permittivity (square) and dielectric losses (triangle) of the KNNSr thick films sintered at 1100 °C in oxygen for a) 2 hours (□, Δ, KNNSr-2h) and b) 4 hours (■, ▲, KNNSr-4h).

tively, for KNNSr-2h against 280 and 0.13, respectively for KNNSr-4h samples. The increased permittivity may be related to the increased density of the thick film. The increased losses at low frequencies are presumably related to the increased electrical conductivity in the sample. This may be due to the increased amount of secondary phases and/or to the humidity during the dielectric measurement which can strongly impact the dielectric permittivity and losses at low frequencies (under 10 kHz) in strontium doped KNN ceramics [31].

The piezoelectric and electromechanical properties of KNNSr-2h and KNNSr-4h are presented in Table 2. The experimental and theoretical complex impedances of the KNNSr-2h sample are presented in Figure 5, showing the good agreement between the adjusted KLM scheme and the experimental data.

For both KNNSr-2h and KNNSr-4h samples, high  $d_{33}$  coefficients around 80 pC/N were obtained. Similar electromechanical properties for KNNSr-2h and KNNSr-4h samples were measured with  $k_t$  up to 35 %. Dielectric constant,  $k_t$  and  $d_{33}$  of the thick films were lower than the one of the processed KNNSr bulk ceramics, which is related to the lower density of the thick films, their deviation from the stoichiometry KNN, and the polyni-

**Figure 5:** Complex electrical impedance (Re(Z): real part, Im(Z): imaginary part) of KNNSr-2h thick film on platinized alumina substrate as a function of the frequency around fundamental resonance (■: experimental; —: theoretical).

obate phase. The thick films electromechanical properties were similar to values reported in the literature [32]. This demonstrates that the thick films prepared by EPD were at the state of the art in terms of electromechanical properties.

#### 4 Summary

KNNSr thick films have been processed by EPD on platinized alumina substrates using a two steps deposition method followed by sintering at 1100 °C in oxygen for 2 and 4 hours. The structural, microstructural, dielectric and electromechanical properties have been reported. The increasing sintering time from 2 to 4 hours leads to higher density, and reduction in unit cell parameters which was related to the formation of a polyniobate phase and the volatilization of alkali oxides. Dielectric constant of the thick film sintered for 4 hours was 280 at 100 kHz and room temperature which is higher value compared to the samples sintered for 2 hours and in agreement with its increased density. The electromechanical performance stayed relatively stable with  $k_t$  up to 35 % and  $d_{33}$  up to 80 pC/N.

## 5 Acknowledgment

This work was supported by the Slovenian Research Agency (P2-0105), the French Research Agency (ANR 14-LAB5-004), the bilateral project BI-FR-16-17-PROTEUS-009/PHC PROTEUS 2016 (No. 35246NJ) and the Erasmus+ programme. The authors would like to thank the Center of Excellence NAMASTE for the use of equipment, Jena Cilenšek, Silvo Drnovšek, Maja Majcen and Hafsa Znibrat for their technical assistance.

## 6 Literature

1. R.M. Ferdous, A.W. Reza, M.F. Siddiqui, Renewable energy harvesting for wireless sensors using passive RFID tag technology: A review, *Renew. Sustain. Energy Rev.* 58 (2016) 1114–1128.
2. H. Kim, Y. Tadesse, S. Priya, Piezoelectric energy harvesting, in: S. Priya, D.J. Inman (Eds.), *Springer US* (2009) 3–39.
3. M.-G. Kang, W.-S. Jung, C.-Y. Kang, S.-J. Yoon, Recent Progress on PZT Based Piezoelectric Energy Harvesting Technologies, *Actuators*. 5 (2016).
4. B. Malič, J. Koruza, J. Hreščak, J. Bernard, K. Wang, J.G. Fisher, A. Benčan, Sintering of lead-free piezoelectric sodium potassium niobate ceramics, *Materials (Basel)*. 8 (2015) 8117–8146.
5. B. Malic, J. Bernard, J. Holc, M. Kosec, Strontium Doped  $K_{0.5}Na_{0.5}NbO_3$  Based Piezoceramics, *Ferroelectrics*. 314 (2005) 149–156.
6. M.D. Maeder, D. Damjanovic, N. Setter, Lead free piezoelectric materials, *J. Electroceramics*. 13 (2004) 385–392.
7. G. Ferin, T. Hoang, C. Bantignies, H. Le Khanh, E. Flesch, A. Nguyen-dinh, Powering autonomous wireless sensors with miniaturized piezoelectric based energy harvesting devices for NDT applications, *IEEE Int. Ultrason. Symp.* (2015) 3–6.
8. I. Coondoo, N. Panwar, H. Maiwa, A.L. Kholkin, Improved piezoelectric and energy harvesting characteristics in lead-free  $Fe_2O_3$  modified KNN ceramics, *J. Electroceramics*. 34 (2015) 255–261.
9. L. Besra, M. Liu, A review on fundamentals and applications of electrophoretic deposition (EPD), *Prog. Mater. Sci.* 52 (2007) 1–61.
10. M. Dolhen, A. Mahajan, R. Pinho, M.E. Costa, G. Trol-liard, P.M. Vilarinho, Sodium potassium niobate ( $K_{0.5}Na_{0.5}NbO_3$ , KNN) thick films by electrophoretic deposition, *RSC Adv.* 5 (2014) 4698–4706.
11. A. Mahajan, R. Pinho, M. Dolhen, M.E. Costa, P.M. Vilarinho, Unleashing the full sustainable potential of thick films of lead-free potassium sodium niobate ( $K_{0.5}Na_{0.5}NbO_3$ ) by aqueous electrophoretic deposition, *Langmuir*. 32 (2016) 5241–5249.
12. H. Mercier, B. Malič, H. Uršič, J. Hreščak, F. Levasort, D. Kuscer, Electrophoretic deposition and properties of strontium-doped sodium potassium niobate thick films, *J. Eur. Ceram. Soc.* 37 (2017) 5305–5313.
13. R. k. Bordia, R. Raj, Sintering Behavior of Ceramic Films Constrained by a Rigid Substrate, *J. Am. Ceram. Soc.* 68 (1985) 287–292.
14. G.W. Scherer, T. Garino, Viscous Sintering on a Rigid Substrate, *J. Am. Ceram. Soc.* 68 (1985) 216–220.
15. R.K. Bordia, A. Jagota, Crack Growth and Damage in Constrained Sintering Films, *J. Am. Ceram. Soc.* 76 (1993) 2475–2485.
16. F. Rubio-marcos, J.F. Fernández, Role of sintering time, crystalline phases and symmetry in the piezoelectric properties of lead-free KNN-modified ceramics, *Mater. Chem. Phys.* (2010).
17. X. Vendrell, J.E. García, F. Rubio-marcos, D.A. Ochoa, L. Mestres, J.F. Fernández, Exploring different sintering atmospheres to reduce nonlinear response of modified KNN piezoceramics, *J. Eur. Ceram. Soc.* 33 (2013) 825–831.
18. K.N. Li, X. Vendrell, L. Mestres, Optimization of the sintering conditions of the  $[(K_{0.5}Na_{0.5})_{1-x}Li_x]NbO_3$  system, *Phys. Procedia*. 8(2010) 57–62.
19. N.M. Hagh, B. Jadidian, A. Safari, Property-processing relationship in lead-free (K, Na, Li)  $NbO_3$ -solid solution system, *J. Electroceramics*. 18(2007) 339–346.
20. K. Kerman, M. Abazari, E.K. Akdo, A. Safari, Lead Free (K, Na) $NbO_3$ -based Piezoelectric Ceramics and Transducers, 17<sup>th</sup> IEEE Int. Symp. Appl. Ferroelectr. 3 (2008) 1–3.
21. J. Hreščak, B. Malič, J. Cilenšek, A. Benčan, Solid-state synthesis of undoped and Sr-doped  $K_{0.5}Na_{0.5}NbO_3$ : Study by thermal analysis and in situ high-temperature X-ray diffraction, *J. Therm. Anal. Calorim.* (2016).
22. International Centre for Diffraction Data. PDF-ICDD, PCPDFWin Version 2.2. June 2001. Newtown Square; 2002. p. Newtown Square, PA.
23. R. Krimholtz, D.A. Leedom, G.L. Matthaei, New Equivalent Circuits for Elementary Piezoelectric Transducers, *Electron. Lett.* 6 (1970) 398–399.
24. A.R. Selfridge, Approximate material properties in isotropic materials, *IEEE Trans. Sonics Ultrason.* 32 (1985) 381–394.
25. A. Jagota, C.Y. Hui, Mechanics of sintering thin films — II. Cracking due to self-stress, *Mech. Mater.* 11 (1991) 221–234.
26. K.B. Singh, M.S. Tirumkudulu, Cracking in Drying Colloidal Films, *Phys. Rev. Lett.* 98 (2007) 218302.
27. J. Hreščak, G. Dražič, M. Deluca, I. Arčon, A. Kodre, M. Dapiaggi, T. Rojac, B. Malič, A. Bencan, Donor doping of  $K_{0.5}Na_{0.5}NbO_3$  ceramics with strontium

- and its implications to grain size, phase composition and crystal structure, *J. Eur. Ceram. Soc.* 37(2017) 2073-2082.
28. A.B. Haugen, F. Madaro, L. Bjørkeng, T. Grande, M. Einarsrud, Sintering of sub-micron  $K_{0.5}Na_{0.5}NbO_3$  powders fabricated by spray pyrolysis, *J. Eur. Ceram. Soc.* 35(2015) 1449-1457.
  29. A. Popovič, L. Bencze, J. Koruza, B. Malič, Vapour pressure and mixing thermodynamic properties of the  $KNbO_3-NaNbO_3$  system, *RSC Adv.* 5 (2015) 76249–76256.
  30. J. Tellier, B. Malic, B. Dkhil, D. Jenko, J. Cilensek, M. Kosec, Crystal structure and phase transitions of sodium potassium niobate perovskites, *Solid State Sci.* 11 (2009) 320–324.
  31. V.Y. Shur, A.A. Esin, D.O. Alikin, A.P. Turygin, A.S. Abramov, J. Hre, A. Bencan, B. Malic, A.L. Kholkin, V.Y. Shur, Ceramics dielectric relaxation and charged domain walls in  $(K,Na) NbO_3$ -based ferroelectric ceramics, 74101 (2017).
  32. F. Levassort, J.-M. Gregoire, M. Lethiecq, K. Astafiev, L. Nielsen, R. Lou-Moeller, W.W. Wolny, High frequency single element transducer based on pad-printed lead-free piezoelectric thick films, in: *IEEE International Ultrasonics Symposium*, (2011) 848–851.

Arrived: 31. 08. 2017

Accepted: 22. 11. 2017



# Design of Operational Transconductance Amplifier with Temperature Compensation

Damjan Berčan, Aleksander Sešek, Janez Trontelj

University of Ljubljana, Faculty of Electrical Engineering, Laboratory for Microelectronics

**Abstract:** In this paper an operational transconductance amplifier [1] with temperature compensation is presented. It is a voltage-controlled current source, which operates in an open loop configuration with a single output connected to a resistive load. The amplifier is internally compensated to keep the gain stable over the  $-40\text{ }^{\circ}\text{C}$  to  $125\text{ }^{\circ}\text{C}$  temperature range. It features low input voltage noise and operates at supply voltages from 3 V to 5.5 V. Additionally, an internal 1.21 V bandgap reference is used to ensure a stable internal voltage reference point. The active area of the proposed integrated circuit designed with  $0.18\text{ }\mu\text{m}$  Bipolar, CMOS, DMOS (BCD) technology is  $750\text{ }\mu\text{m} \times 260\text{ }\mu\text{m}$ . It consumes  $423\text{ }\mu\text{A}$  of current and it has  $8.87\text{ nV}/\sqrt{\text{Hz}}$  of input noise at 500 kHz. The resulting simulated voltage gain is 40 dB and variations are less than  $\pm 0.3\text{ dB}$  over the temperature range of  $-40\text{ }^{\circ}\text{C}$  to  $125\text{ }^{\circ}\text{C}$ .

**Keywords:** Operational Transconductance Amplifier; Temperature compensated bias current; Temperature sensitivity optimization

## Načrtovanje operacijskega transkonduktančnega ojačevalnika s temperaturno kompenzacijo

**Izvleček:** V članku je predstavljen transkonduktančni ojačevalnik s temperaturno kompenzacijo. Na izhod odprto-zančnega ojačevalnika oziroma napetostno krmiljenega tokovnega vira je priključeno uporabno breme. Notranja kompenzacija skrbi za stabilno ojačenje v temperaturnem območju od  $-40\text{ }^{\circ}\text{C}$  do  $125\text{ }^{\circ}\text{C}$ . Poleg tega ojačevalnik izkazuje majhen vhodni šum in deluje v napetostnem območju od 3 V do 5.5 V. Vezje vsebuje napetostno referenco, ki poskrbi za stabilno referenčno točko. Integrirano vezje je bilo načrtano v  $0.18\text{ }\mu\text{m}$  BCD (Bipolar, CMOS, DMOS) tehnologiji, njegova aktivna površina znaša  $750\text{ }\mu\text{m} \times 260\text{ }\mu\text{m}$ . Poraba ojačevalnika znaša  $423\text{ }\mu\text{A}$ , njegova šumna gostota na vhodu je  $8.87\text{ nV}/\sqrt{\text{Hz}}$  pri frekvenci 500 kHz. Napetostno ojačenje znaša 40 dB in v temperaturnem območju od  $-40\text{ }^{\circ}\text{C}$  do  $125\text{ }^{\circ}\text{C}$  odstopa za manj kot  $\pm 0.3\text{ dB}$ .

**Ključne besede:** Transkonduktančni operacijski ojačevalnik; temperaturna kompenzacija delovnega toka; optimizacija temperaturne občutljivosti

\* Corresponding Author's e-mail: damjan.bercan@fe.uni-lj.si

### 1 Introduction

In the paper, an integrated circuit including a symmetrical Operational Transconductance Amplifier (OTA) with temperature compensation is described. The OTA can be presented as a voltage controlled current source. The ideal OTA has very high input and output impedances and a wide frequency bandwidth. The output current  $I_{OUT}$  is proportional to the differential input voltage and is expressed as:

$$I_{OUT} = g_m V_d \quad (1)$$

where  $g_m$  is the transconductance of the amplifier and  $V_d$  is the differential input voltage.

One of the major drawbacks of the OTA is its high temperature sensitivity, caused by inversely proportional temperature variations of  $g_m$  [2, 3]. Transconductance of the Metal-Oxide-Semiconductor (MOS) transistor, using small signal model in saturation region is defined as follows:

$$g_m = \sqrt{2\mu_n C_{ox} \left(\frac{W}{L}\right) I_D} \quad (2)$$

where  $\mu_n$  is carrier mobility,  $C_{ox}$  is oxide capacitance,  $W$  is width of the device,  $L$  is length of the channel and  $I_D$  is drain current [4].

The root cause of temperature variations is the temperature dependent threshold voltage  $V_T$  and the carrier mobility  $\mu_n$  variations of the MOS transistor, according to equations (2) and (3):

$$V_T(T) = V_T(T_0) + \alpha_{VT}(T - T_0) \tag{3}$$

$$\mu_n(T) = \mu_n(T_0) \left( \frac{T}{T_0} \right)^{\alpha_\mu} \tag{4}$$

where  $T_0$  is the reference temperature (300 °K),  $\alpha_{VT}$  and  $\alpha_\mu$  are negative values which vary with temperature [5]. As one of possible solutions, a circuit with output voltage Proportional To Absolute Temperature (PTAT) can be implemented to compensate the temperature variations of  $g_m$ . The difference between the two base-emitter voltages in PTAT is expressed as:

$$\Delta V_{BE} = V_t \ln(J_2 / J_1) \tag{5}$$

where  $V_t$  is thermal voltage and  $J_1, J_2$  are different current densities of bipolar transistors. The PTAT circuit generates voltage which has a positive Temperature Coefficient (TC) [4].

The following section (Section 2) presents the OTA design method to overcome the mentioned problem. In section 3, simulation results for typical simulation conditions, process variations and Monte Carlo analyses are presented.

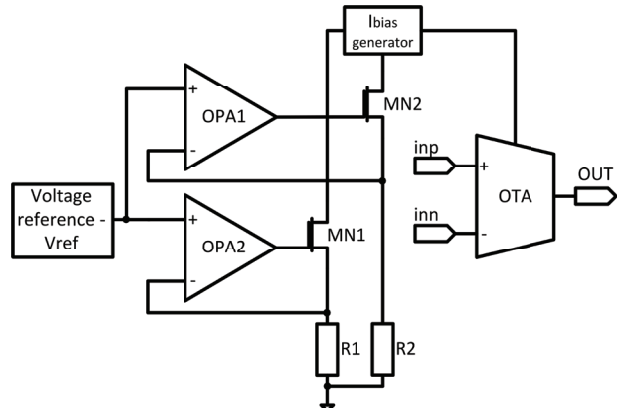


Figure 1: Block diagram of integrated circuit.

## 2 Ota circuit design

The block diagram of the OTA with temperature compensation is shown in Fig.1. The main advantage of the proposed solution is the temperature compensated bias current. The compensation circuit consists of two resistors (R1 and R2) having different TC. The block diagram also includes internal a 1.21 V voltage reference ( $V_{ref}$ ), biasing current generator ( $I_{bias}$  generator) which compensate the temperature variations of  $g_m$ , two Operational Amplifiers (OPA1 and OPA2) for voltage to current conversion and OTA circuit. Our objective was to keep the gain of the OTA stable over the -40 °C to

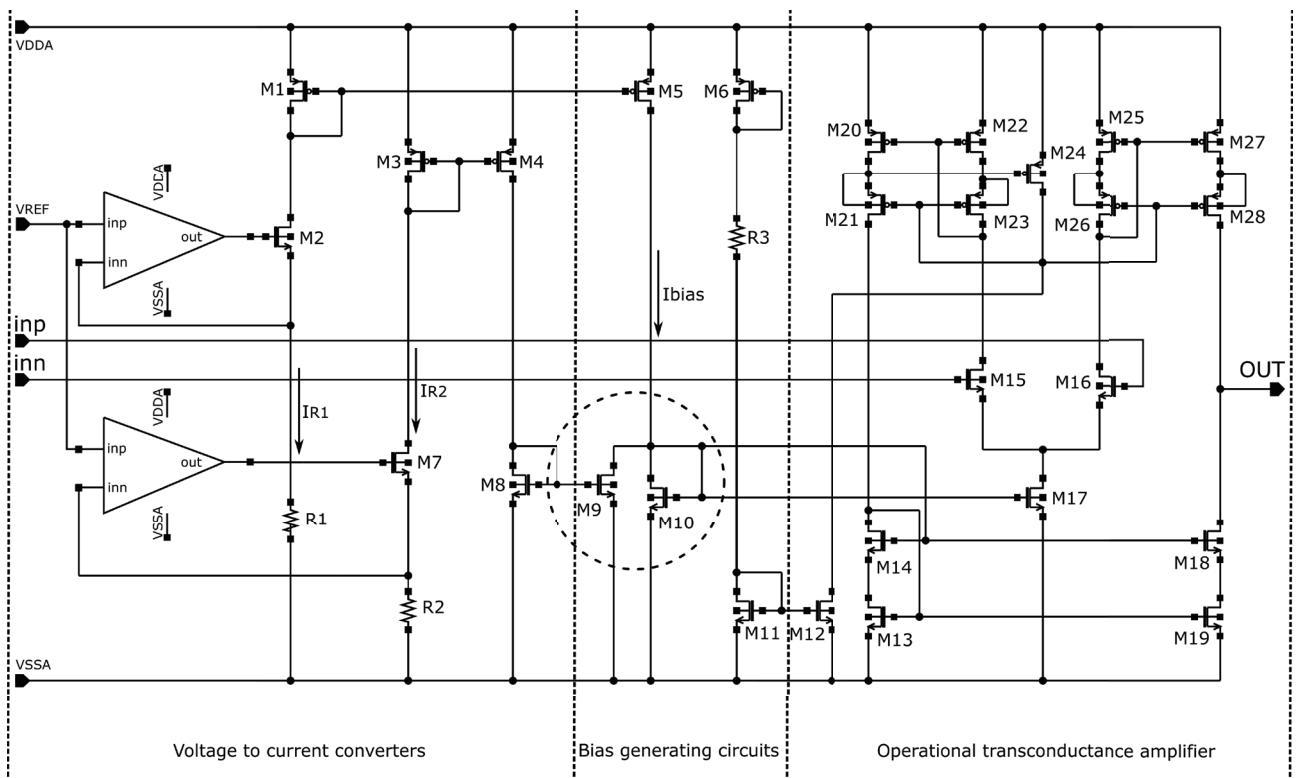
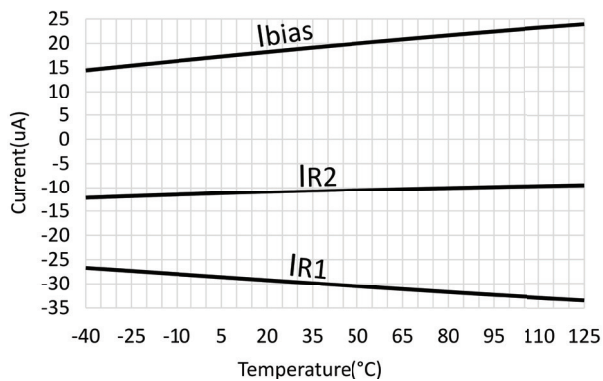


Figure 2: The schematic of integrated circuit.



**Figure 3:** Generated currents.

125 °C temperature range, low input voltage noise and high Power Supply Rejection Ratio (PSRR).

### 2.1 Topology of the circuit

The schematic of the balanced OTA with temperature compensation is shown in the Fig. 2. The voltage to currents converters are used to convert the reference bandgap voltage to the corresponding current. Both converters are designed as classic two stage amplifiers with a N type Metal-Oxide-Semiconductor (NMOS) input differential stage and a common source output stage including compensation capacitor and resistor. To ensure precise conversion, the temperature stable reference voltage is employed. The voltage reference - bandgap circuit, maintains a stable voltage over the temperature range and power supply voltage variations. The OTA consists of NMOS input differential stage and three current mirrors. Transistors M20 – M23 form the first current mirror stage, M25 – M28 form the second current mirror stage and M13, M14, M18 and M19 form the third current mirror stage. To increase the output impedance the cascode current mirrors are used. The gate of transistors are connected and biased as low voltage cascode, which keeps the minimum drain source voltages of transistor M13, M22 and M25 and also insures transistor saturation operation. The Length (L) of transistor M10 is higher in order to compensate the body effect of cascode transistors M14 and M18 [6].

### 2.4 Compensation circuit

The compensation circuit consists of transistors M9 and M10 and two resistors (R1 and R2) with different TC, which is calculated using the box-method [7], -1618 ppm/°C and 1322 ppm/°C, respectively. The Fig. 3 presents the currents  $I_{R1}$  and  $I_{R2}$  determined by resistors R1 and R2, and bias current  $I_{bias}$  flowing through M10.

The compensation circuit generates bias current  $I_{bias}$  which is stated as:

$$I_{bias} = -I_{R1} + I_{R2} \tag{6}$$

The bias current  $I_{bias}$  increases with temperature compensating decreasing transconductance of OTA.

## 3 Simulation results

### 3.2 Results for typical simulation parameters

The typical process parameters simulations at 25 °C were performed for the supply voltages 3.3 V and 5 V, respectively. The simulation results are presented in Table 1. Input noise density was measured at 500 kHz.

**Table 1:** Simulation results at typical simulation conditions.

Param. \ Suppl.	3.3 V	5 V	Units
Ivdda	423	540	µA
G	40.2	40.4	dB
BW	13.6	15.0	MHz
Input noise density	8.87	8.56	nV/√Hz
Input offset voltage	1.08	1.99	mV
CMRR	-132	-142	dB
+SR	9.01	9.60	V/µs
-SR	9.23	9.72	V/µs
PSRR @ 100 Hz	-73.5	-78.2	dB
Transconductance	778	737	µA/V

The input referred noise voltage can be further reduced by changing the channel W/L ratio of the M15 and M16 transistors or increasing the bias current  $I_{bias}$ . This action would lead to larger chip area (higher cost) and higher power consumption. To reduce the offset which effects the performance of the OTA, the auto-zeroing or chopping technique method could be used, adding complexity to the design. Precise matching strategies of the transistors and resistors devices must be used to minimize offsets and provide symmetry.

Typical performance characteristics for a 3.3 V supply voltage are shown from Figures 4 to 7. The input referred noise voltage was measured at 500 kHz, while PSRR was measured at 100 Hz.

Fig. 4 shows the voltage gain vs. frequency at three temperatures (-40 °C, 25 °C, 125°C), which is 40 dB. The results show that the gain sensitivity to temperature variations are almost eliminated with the presented design. The bandwidth of the OTA varies from 14.1 MHz at -40 °C to 12.8 MHz at 125 °C.

**Table 2:** Corner analysis results

Parameters	FF1	SS1	FS1	SF1	FF2	SS2	FS2	SF2	Units
Ivdda	485	374	430	416	621	476	550	530	μA
G	41.3	39.2	40.2	40.1	41.5	39.4	40.45	40.32	dB
BW	14.5	12.6	13.8	13.3	16.0	14.0	15.2	14.7	MHz
Input noise density	8.25	9.43	8.81	8.92	7.95	9.13	8.50	8.62	nV/√Hz
Offset	1.57	0.71	1.16	1.00	2.72	1.37	2.11	1.89	mV
CMRR	-132	-130	-134	-129	-140	-144	-141	-143	dB
+SR	10.28	8.02	9.06	8.95	10.97	8.54	9.66	9.54	V/μs
-SR	10.54	8.19	9.3	9.13	11.1	8.65	9.79	9.66	V/μs
PSRR @ 100 Hz	-68.9	-78.5	-75.3	-72.1	-73.8	-83.5	-81.3	-75.8	dB
Transconductance	856	715	785	770	816	672	737	737	μA/V

Note<sup>1</sup>: Supply voltage: 3.3 V

Note<sup>2</sup>: Supply voltage: 5 V

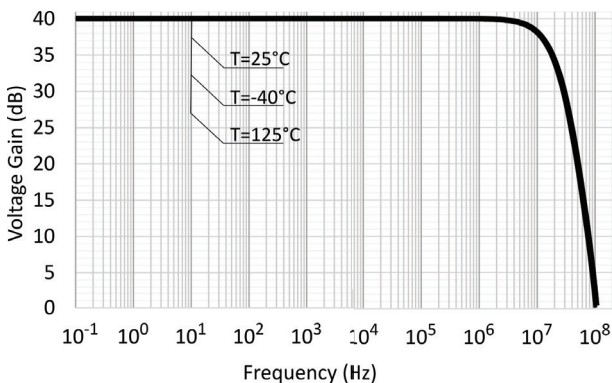


**Figure 4:** Voltage Gain vs. Frequency

Fig. 5 presents input referred noise voltage density as a function of frequency at temperatures (-40 °C, 25 °C, 125 °C). The noise measured at 500 kHz increases with temperature from 8.16 nV/√Hz at -40 °C to 10.1 nV/√Hz at 125 °C.

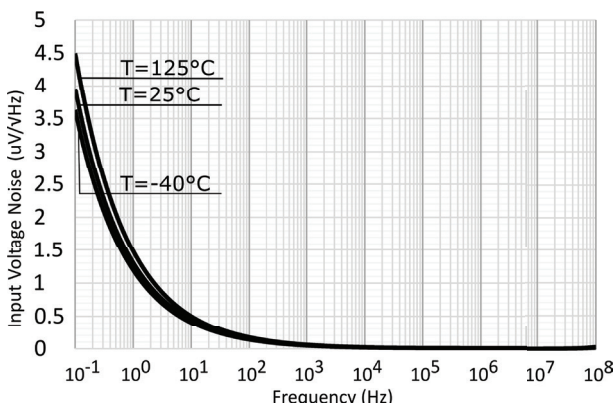


**Figure 5:** Input Noise Voltage vs. Frequency

The Common Mode Rejection Ratio (CMRR) is measured as the ratio of the common mode gain to differ-

ential mode gain. At lower frequencies the CMRR varies from -131 dB at -40 °C to -121 dB at 125 °C. The results are shown in Fig. 6.

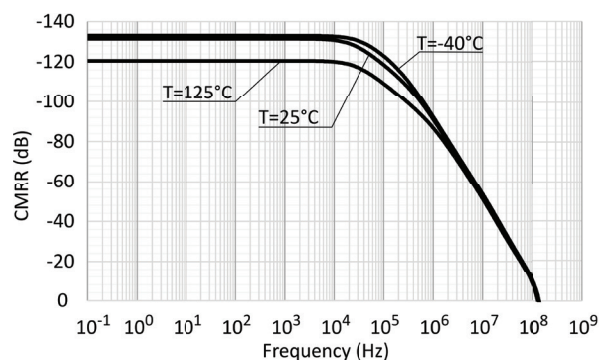


**Figure 6:** CMRR vs. Frequency

The PSRR is measured as the ratio of the OTA output variation vs. the supply voltage variation regardless the input signal. The PSRR varies from -78.2 dB at -40 °C to -62.9 dB at 125 °C, measured at 100 Hz. At higher frequencies, PSRR deteriorates. The results are shown in Fig. 7.

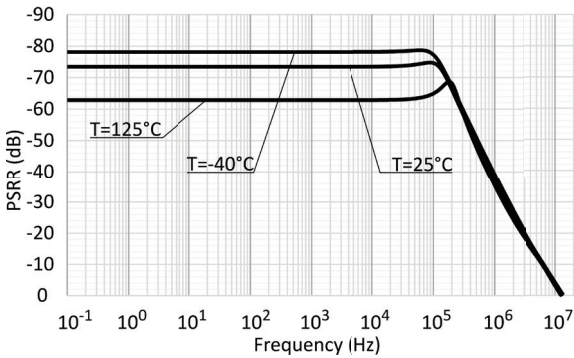
### 3.2.1 Corner analysis

The process variations of MOSFETs and resistors influence on performance of fabricated integrated circuit. Therefore, the OTA was simulated for different process corners – four corner models (FF, SS, FS and SF). The results at 25 °C are gathered in Table 2. The input noise density was measured at 500 kHz.

### 3.2.2 Monte Carlo simulation

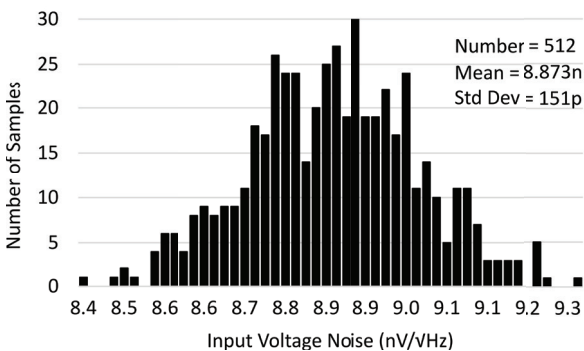
In this section the results of the Monte Carlo (MC) analysis are shown. The MC simulations were performed

including mismatch and process variations at typical conditions (25 °C and 3.3 V) comprising 512 MC runs. The simulation results are presented in the following histograms.



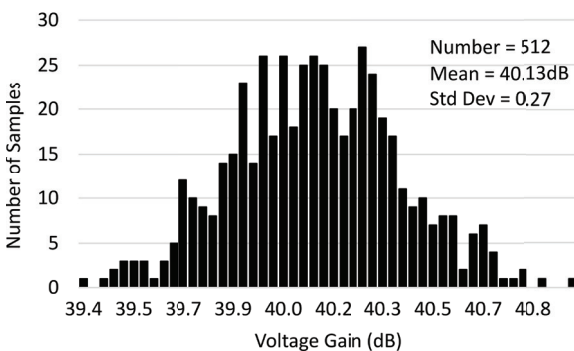
**Figure 7:** PSRR vs. Frequency

Fig. 8 shows the resulting histogram of input referred noise density at 500 kHz, which has a mean value of 8.873 nV/√Hz and the standard deviation of 151 pV/√Hz. The result is a bit higher than the mean value of previously shown corner analysis results, which is 8.853 nV/√Hz.



**Figure 8:** MC test of Input Voltage Noise

The voltage gain distribution is shown in the Fig. 9. The mean value from the corner analysis results is 40.20 dB



**Figure 9:** MC test of Voltage Gain

and it is slightly higher than the mean value obtained by MC analysis, which is 40.13 dB with a standard deviation of 0.27 dB.

The offset voltage mean value from MC runs is 1.079 mV with standard deviation of 103.7 uV. It is shown in Fig. 10.

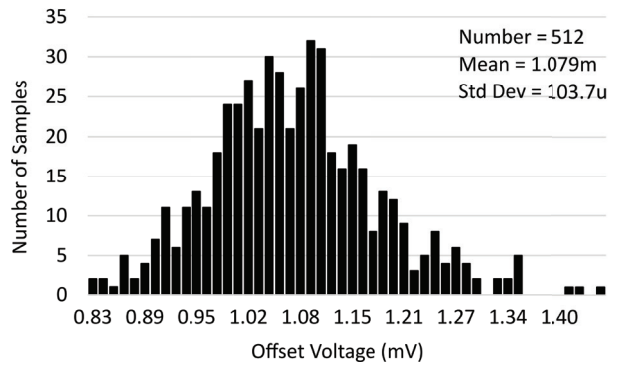


**Figure 10:** MC test of Offset Voltage

The mean value of the voltage offset from corner analysis is 1.110 mV, which is higher than the MC results.

The comparison between corner and MC analyses must be done carefully as the corner analysis comprises also temperature and supply voltage variations, which especially influence voltage offset.

#### 4 Layout of presented circuit

The layout of the presented integrated circuit is shown on Fig. 11.

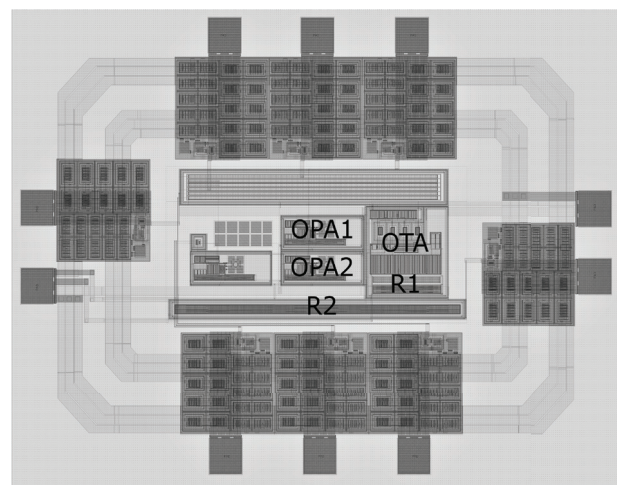


**Figure 11:** Layout of the integrated circuit

The active area of the circuit, without bonding pads and supply connection rings, is  $750\ \mu\text{m} \times 260\ \mu\text{m}$ . The integrated circuit has been designed with the  $0.18\ \mu\text{m}$  BCD technology as a part of the System on Chip (SoC). The BCD technology allows mixed - signal design using low and high voltage transistors (DMOS) on the same die (reduces cost, area and power consumption). The voltage to current converter main part is presented by resistors R1 – N+ poly without salicide and R2 – N+ diffusion without salicide, which means that resistors do not have an additional process mask of salicide, reducing the sheet resistance ( $\Omega/\text{sq}$ ) of the resistors. For ASIC area reduction, N – well resistors could be used, but they have high nonlinearity and larger parasitic capacitance between N – well and substrate. The integrated circuit has been sent to the fabrication factory.

## 5 Conclusions and next steps

The OTA was designed and analyzed using the  $0.18\ \mu\text{m}$  BCD technology. The temperature sensitivity of the OTA has been optimized and reduced, using the bias control technique and a stable internal voltage reference. The proposed circuit shows voltage gain variations lower than  $\pm 0.3\ \text{dB}$  in the temperature range from  $-40\ ^\circ\text{C}$  to  $125\ ^\circ\text{C}$  and lower than  $0.5\ \text{dB}$  when varying the supply voltage in the range from  $3\ \text{V}$  to  $5.5\ \text{V}$ . The equivalent input referred noise voltage is simulated to be lower than  $10\ \text{nV}/\sqrt{\text{Hz}}$  at  $500\ \text{kHz}$  and  $25\ ^\circ\text{C}$ , and voltage offset lower than  $2.8\ \text{mV}$ . To overcome the problem of process variations, especially the resistors R1 and R2 which are used for compensation current generation and are one of the most critical elements in compensations circuit, the resistance of both R1 and R2 resistors will be precisely trimmed. The issue could be easily solved by employing effective and uncomplicated trimming resistor stage for each of them separately and internal One-Time-Programmable (OTP) memory cells.

## 6 References

1. W. M. C. Sansen, *Analog Design Essentials*, let. 2006. Springer US.
2. W. Surakampontorn, V. Riewruja, K. Kumwachara, C. Surawatpunya, in K. Anuntahirunrat, „Temperature-insensitive voltage-to-current converter and its applications“, *IEEE Trans. Instrum. Meas.*, let. 48, št. 6, str. 1270–1277, dec. 1999.
3. T. Parveen, *A textbook of operational transconductance amplifier and analog integrated circuits*. New Delhi: I. K. International Publishing House, 2012.
4. A. Pleteršek, *Načrtovanje analognih integriranih vezij v tehnologijah CMOS in BiCMOS*. Ljubljana: Fakulteta za elektrotehniko, 2006.
5. I. M. Filanovsky in A. Allam, „Mutual compensation of mobility and threshold voltage temperature effects with applications in CMOS circuits“, *IEEE Trans. Circuits Syst. Fundam. Theory Appl.*, let. 48, št. 7, str. 876–884, jul. 2001.
6. T. C. Carusone, K. W. Martin, in D. Johns, *Analog integrated circuit design, 2nd edition*. Hoboken, N.J.: John Wiley & Sons, 2011.
7. M. E. T. Instruments, „Voltage Reference Selection Basics“. Available at: <http://www.ti.com/lit/wp/slpy003/slpy003.pdf>. Accessed: [6.8.2016]

Arrived: 31. 08. 2017

Accepted: 11. 12. 2017

# *Boards of MIDEM Society | Organi društva MIDEM*

## *MIDEM Executive Board | Izvršilni odbor MIDEM*

### **President of the MIDEM Society | Predsednik društva MIDEM**

Prof. Dr. Marko Topič, University of Ljubljana, Faculty of Electrical Engineering, Slovenia

### **Vice-presidents | Podpredsednika**

Prof. Dr. Barbara Malič, Jožef Stefan Institute, Ljubljana, Slovenia

Dr. Iztok Šorli, MIKROIKS, d. o. o., Ljubljana, Slovenija

### **Secretary | Tajnik**

Olga Zakrajšek, UL, Faculty of Electrical Engineering, Ljubljana, Slovenija

### **MIDEM Executive Board Members | Člani izvršilnega odbora MIDEM**

Darko Belavič, In.Medica, d.o.o., Šentjernej, Slovenia

Dr. Slavko Bernik, Jožef Stefan Institute, Ljubljana, Slovenia

Dr. Miha Čekada, Jožef Stefan Institute, Ljubljana, Slovenia

Prof. DDr. Denis Donlagič, UM, Faculty of Electrical Engineering and Computer Science, Maribor, Slovenia

Prof. Dr. Leszek J. Golonka, Technical University Wroclaw, Poland

Dr. Vera Gradišnik, Tehnički fakultet Sveučilišta u Rijeci, Rijeka, Croatia

Leopold Knez, Iskra TELA d.d., Ljubljana, Slovenia

mag. Mitja Koprivšek, ETI Elektroelementi, Izlake, Slovenia

Prof. Dr. Miran Mozetič, Jožef Stefan Institute, Ljubljana, Slovenia

Prof. Dr. Janez Trontelj, UL, Faculty of Electrical Engineering, Ljubljana, Slovenia

Dr. Danilo Vrtačnik, UL, Faculty of Electrical Engineering, Slovenia

## *Supervisory Board | Nadzorni odbor*

Prof. Dr. Franc Smole, UL, Faculty of Electrical Engineering, Ljubljana, Slovenia

prof. dr. Drago Strle, UL, Faculty of Electrical Engineering, Ljubljana, Slovenia

Igor Pompe, Ljubljana, Slovenia

## *Court of honour | Častno razsodišče*

Emer. Prof. Dr. Jože Furlan, Slovenia

Dr. Marko Hrovat, Slovenia

Dr. Miloš Komac, Slovenia

**Informacije MIDE**  
*Journal of Microelectronics, Electronic Components and Materials*  
ISSN 0352-9045

*Publisher / Založnik:*  
*MIDEM Society / Društvo MIDE*  
*Society for Microelectronics, Electronic Components and Materials, Ljubljana, Slovenia*  
Strokovno društvo za mikroelektroniko, elektronske sestavne dele in materiale, Ljubljana, Slovenija

[www.midem-drustvo.si](http://www.midem-drustvo.si)